

1
2
3
4
5
6
7
8
9
10
11
12
13
14
15
16
17
18
19
20
21
22
23
24
25
26
27
28
29
30
31
32
33

A multimodal approach to identify clinically relevant parameters to monitor disease progression in a preclinical model of neuropediatric disease

Authors: Tyler B. Johnson^{1†}, Jon J. Brudvig^{1†}, Kimmo K. Lehtimäki², Jacob T. Cain¹, Katherine A. White¹, Timo Bragge², Jussi Rytönen², Tuulia Huhtala², Derek Timm¹, Maria Vihma², Jukka T. Puoliväli², Antti Nurmi^{2*}, Jill M. Weimer^{1,3*}

Affiliations:

¹Pediatrics and Rare Diseases Group, Sanford Research, Sioux Falls, SD 57104, USA.

²Discovery Research Services, Charles River, Kuopio, Finland.

³Department of Pediatrics, Sanford School of Medicine at the University of South Dakota, Sioux Falls, SD 57104, USA.

*To whom correspondence should be addressed: jill.weimer@sanfordhealth.org and antti.nurmi@crl.com

†Authors contributed equally

One Sentence Summary: Principal component analysis identifies a set of clinically relevant parameters able to measure progression of Batten disease in a mouse model.

Abstract: While research has accelerated the development of new treatments for pediatric neurodegenerative disorders, the ability to demonstrate the long-term efficacy of these therapies has been hindered by the lack of convincing, noninvasive methods for tracking disease progression both in animal models and in human clinical trials. Here, we unveil a new translational platform for tracking disease progression in an animal model of a pediatric neurodegenerative disorder, CLN6-Batten disease. Instead of looking at a handful of parameters or a single “needle in a haystack”, we embrace the idea that disease progression, in mice and patients alike, is a diverse phenomenon best characterized by a combination of relevant biomarkers. Thus, we employed a multi-modal quantitative approach where 144 parameters were longitudinally monitored to allow for individual variability. We use a range of noninvasive neuroimaging modalities and kinematic gait analysis, all methods that parallel those commonly used in the clinic, followed by a powerful statistical platform to identify key progressive anatomical and metabolic changes that correlate strongly with the progression of pathological and behavioral deficits. This innovative, highly sensitive platform can be used as a powerful tool for preclinical studies on neurodegenerative diseases, and provides proof-of-principle for use as a potentially translatable tool for clinicians in the future.

34 **[Main Text:]**

35 **Introduction**

36 Rare diseases, conditions that affect fewer than 200,000 patients in the U.S. or less than 1 in 2,000 people in the EU (1),
37 represent a particular challenge for medical diagnosis as clinical features are often complex and enigmatic. While very few rare
38 diseases have effective treatments, resulting from the limited information that is typically available for many of these conditions,
39 access to improved animal models and state-of-the art medical diagnostic capabilities are helping to accelerate the number of clinical
40 trials and treatments available to patients. Due to their rarity, access to patients is particularly limited, so researchers and clinicians
41 must rely on comprehensive natural history studies that provide a snapshot of where a typical patient would exist in time. Moreover,
42 because many of these diseases are pediatric and ultimately fatal, the Rare Diseases Act of 2002 made it possible to accelerate the
43 clinical trial design process, with one concession being that the trial need not include untreated controls, thus making the natural
44 history data even more essential. Although much attention has been focused on collecting this information, much of what is captured
45 can be subjective and qualitative. Thus, quantitative biomarkers that can be monitored longitudinally and are minimally invasive are
46 greatly needed in order to monitor treatment responses in both preclinical animal models and human clinical trials. Translational
47 utilization of animal models of human disease benefits greatly from relevant phenotypic characterization. Unfortunately, the
48 techniques most commonly used in animal models often suffer from a lack of translatability. Behavioral assays for mice most often
49 focus on murine-relevant behaviors that are not necessarily applicable to the clinic. Similarly, mouse pathology is typically focused on
50 invasive post-mortem analysis of tissues, processes that are not practiced in human patients. This lack of translatability renders many
51 preclinical phenotypic characterizations difficult to translate to the clinic.

52 Comprehensive noninvasive biomarker panels are not available for many neurodegenerative disorders, and these are of
53 special interest for pediatric disorders, as determining disease progression early on is critical to identifying proper clinical
54 interventions and monitoring responses to potential corrective therapies. Batten disease (i.e., neuronal ceroid lipofuscinoses), a family
55 of lysosomal storage disorders resulting from mutations in one of 13 genes, collectively represents the most common
56 neurodegenerative disease in children (2, 3). Although the functions of many of these genes are unknown, much work in the past
57 decade has been dedicated to developing and testing therapies. With the recent advancements in research tools, including high-
58 throughput and high-content screening methods, the Batten disease scientific community has been progressing toward potential
59 therapies at an unprecedented pace, and as a result, treatments are moving from the preclinical phase to clinical trials more quickly and
60 efficiently than ever before. Also, with such heterogeneous disease states, resulting from different mutations that lead to more
61 aggressive or protracted forms of the disease, clinical research teams are forming large, international collaborations to ensure that
62 comprehensive natural history studies are completed and in place as a resource for all clinical trials. These interdisciplinary groups
63 have paved the way for these natural history studies, led by the DEM-CHILD NCL Patient Database Consortium and the University of
64 Rochester Batten Center (4, 5). Additionally, these groups have developed clinical rating scales to assess cognitive, motor, and
65 behavioral function of patients with Batten disease (6-8). With a growing number of clinical trials for Batten disease therapies, there is
66 an increasing need for noninvasive, clinically-relevant biomarkers to track therapeutic efficacy.

67 To address these needs, we used a mouse model of CLN6 Batten disease to perform an exhaustive multi-factorial
68 characterization of biomarkers, moving away from mouse behavioral assays to clinical outcomes that are congruent to those used in
69 human patients. CLN6 disease is caused by autosomal recessive mutations in *CLN6*, which results in the reduction or complete
70 absence of the CLN6 protein. This disease is characterized by the accumulation of autofluorescent storage material in lysosomes,
71 progressive neurodegeneration throughout cortex and thalamus, as well as massive gliosis throughout the central nervous system
72 (CNS). Patients often present with language deficits, cognitive impairment and progressive motor decline. As the disease progresses,
73 patients lose vision, develop seizures and ultimately succumb to the disease around 10-12 years of life. The spontaneously occurring
74 *Cln6^{ncf}* mouse model of CLN6 disease has been shown to faithfully recapitulate many of the hallmarks of the human disease both
75 behaviorally and pathologically (9, 10), but noninvasive, clinically relevant assays have not yet been employed to characterize
76 longitudinal changes in this model. Various scientists, our lab included, have performed a very comprehensive pathological
77 assessment of Batten disease rodent and large animal models to reveal how different brain regions change over time, however, these
78 experiments were all conducted on post-mortem brain samples (11-20). These studies have shown that brain pathology is present
79 months before any noted behavioral changes, similar to what has been noted in human patients. Thus, cellular changes and
80 degeneration are occurring in the the brain long before one notices any behavior or cognitive changes, so developing more sensitive
81 tools for detecting disease states prior to the onset of behavioral symptoms would be of immense value in the clinic. Our previous
82 work, as well as the work of others, has largely been focused on finding a single biomarker – the elusive “needle in a haystack” -
83 associated with Batten disease and its progression (21-24), but this approach has failed to yield any reliable metrics.

84 In this study, rather than focusing on one or a few metrics, we used multiple imaging modalities as well as a comprehensive
85 gait assessment to track hundreds of parameters over time, and performed a combinatorial analysis to identify a biomarker signature
86 for CLN6-disease. Cohorts of wild type and *Cln6^{ncf}* mice of both sexes were monitored longitudinally using noninvasive imaging,
87 including T2-weighted magnetic resonance imaging (T2-MRI), diffusion tensor MRI (DTI), ¹H magnetic resonance spectroscopy
88 (MRS), and positron emission tomography (PET) was performed periodically between 3-12 months of age while kinematic gait
89 analysis (KGA), which captures a large number of metrics describing gait, was assayed from 6-12 months of age. Variations of all of
90 these techniques are widely used in the clinic and have shown correlations between mouse models and human subjects (25, 26). Once
91 we had characterized these parameters in the CLN6 disease mouse model, we used a recently developed form of principal component
92 analysis (PCA), contrastive PCA (cPCA), to cluster the four imaging modalities and gait analysis in order to derive new variables that

93 best capture and define the progressive nature of the disease. Together, this approach provides a robust and translatable platform for
94 longitudinal monitoring of disease progression that can have profound utility, not only for Batten disease, but in a variety of animal
95 models of rare neuropsychiatric diseases.

96 97 **Results**

98 *Progressive changes in brain volume and anatomy in a model of CLN6 disease.*

99 The selective vulnerability of various populations of neurons is a key feature of many neurodegenerative diseases, including
100 Batten disease (27, 28). Prior studies have demonstrated that thinning of select anatomical regions and different cortical layers is
101 present in *Cln6^{nc/f}* mice (9, 12, 14, 19), however, all of these measurements are based on invasive, histopathological analysis of post-
102 mortem tissues. To identify progressive changes in brain architecture, we examined cohorts of mice longitudinally up to one year of
103 age with T2 weighted magnetic resonance (T2-MRI) and diffusion tensor imaging (DTI).

104 Whole brain volume steadily decreased over time in *Cln6^{nc/f}* mice, with lower volume noted at 6, 9 and 12 months of age with
105 clear differences in unique brain regions (**Fig. 1**). Progressive cortical atrophy began at 9 months and was profound at 12 months,
106 where cortical volume was reduced in size by ~14%. Milder atrophy was also observed in the cerebellum at 12 months, culminating in
107 a ~9% reduction in volume. Interestingly, there was a slight but significant increase in whole brain volume at 3 months of age (~1%).
108 Historically, scientists have focused on one sex or mixed sexes for behavioral and pathological changes rather than analyzing them
109 individually. Here we separated and tracked individual sexes, providing an innovative way of monitoring these animals over time and
110 strengthening the translational utility. Sex differences were also evident, with the increase in whole brain volume at 3 months seen
111 solely in male *Cln6^{nc/f}* mice, but decreasing in both sexes beginning at 6 months of age (**Fig. S1, Table S1**). Cortical atrophy also
112 appeared earlier (at 9 months) in females than in males (at 12 months). In human patients and mouse models of neurodegenerative
113 diseases, such profound cortical atrophy is typically accompanied by an increase in lateral ventricle volume (29). Surprisingly, we did
114 not detect such changes in the *Cln6^{nc/f}* mice. Still, these results suggest progressive neurodegeneration results in multiple changes in
115 brain structure volumes over the time course of the disease.

116 To determine whether reductions in grey matter volume were accompanied by corresponding changes in white matter
117 perturbations, we performed DTI to measure fractional anisotropy (FA) of several major CNS axon tracts. FA as measured by DTI
118 reflects the level of preferred directionality of the diffusion of water molecules. Thus, higher FA values can reflect greater numbers,
119 packing, or diameters of axons, lower variability in axon orientation, or more dense myelination (30). There were varying changes in
120 FA of the forceps minor of the corpus callosum (fmi) over the time points monitored, and a consistent decrease in FA in the anterior
121 portion of the anterior commissure (aca) beginning at 6 months of age (**Fig. 2**). Additionally, there were several regions with a
122 decrease in FA at 12 months of age, correlating with the progressive and profound atrophy occurring at this time point. Within
123 individual sexes, the FA of the fmi was increased in a male specific manner at 6 and 9 months of age (**Fig. S2**). Female *Cln6^{nc/f}* mice
124 showed a decreased in FA in the splenium of the corpus callosum (scc) at 6 months of age, prior to their male counterparts, while both
125 sexes began showing a decrease in FA in the aca beginning at 6 months of age (**Fig. S2, Table S2**). By 12 months of age, both sexes
126 showed decreased FA in several white matter areas. These results demonstrate that progressive white matter defects are also prevalent
127 in *Cln6^{nc/f}* mice, with unique sex specific perturbations in various white matter regions.

128 *Alterations in brain metabolism, metabolites, and markers of brain inflammation associated with CLN6 disease.*

129 Abnormalities in brain metabolism in the form of decreases in glucose uptake and increases in various markers of
130 neuroinflammation is a common signature of a number of neurodegenerative disorders (31, 32). To explore whether such changes are
131 present in the *CLN6*-Batten disease mouse model, we performed ¹H magnetic resonance spectroscopy (MRS) and positron emission
132 tomography (PET) imaging. MRS was first used to examine longitudinal changes in various brain metabolites in the frontal cortex.
133 While we observed subtle changes in a variety of metabolites at various time points, the most significant changes were observed for
134 glutamine (GLN), N-acetylaspartate (NAA), and NAA + N-acetylaspartylglutamic acid (NAA+NAAG) (**Table 1**). GLN levels
135 steadily increased in *Cln6^{nc/f}* mice over time, reaching significantly elevated levels at 12 months of age in both sexes (**Table 1**). NAA
136 and NAA+NAAG levels steadily decreased over time, reaching significantly lower levels at 9 and 12 months of age in both sexes.
137 Additionally, taurine (TAU) was reduced at 3 – 9 months, more prominently in male mice, and creatine (Cr) + phospho-creatine (PCr)
138 reduced at 3 months in female mice, though these differences resolved over time. These results suggest that alterations in glutamate-
139 glutamine cycling and excitatory signaling may be a prominent feature of this disease model, mirroring what has been found in other
140 studies(33). Furthermore, NAA decreases we observed mirror those seen in human patients with a number of neurodegenerative
141 disorders including Batten disease (34-36), suggesting that this may be a useful marker for monitoring neurodegeneration in *Cln6^{nc/f}*
142 mice.

143 To explore potential changes in brain metabolism (i.e. brain glucose utilization), we used PET to monitor uptake of
144 fluorodeoxyglucose (¹⁸F, FDG), a PET-detectable proxy for glucose. At 12 months, where we observed the most severe alterations in
145 brain anatomy, we found that FDG standardized uptake values (SUV) were significantly compromised in all regions examined in male
146 *Cln6^{nc/f}* mice and in many regions in female *Cln6^{nc/f}* mice (**Table 2**). We also utilized PET to measure the uptake of ¹⁸F-FEPPA. This
147 ligand binds the translocator protein (TSPO), which is upregulated in microglia in response to neuroinflammation, one of the earliest
148 reported pathological changes in Batten disease mouse models (37). Interestingly, at 13 months of age, uptake was reduced in male
149 mice in the basal forebrain and septum (BFS), cortex, and olfactory bulb while increased uptake was found in females in the central

gray matter, superior colliculi, and thalamus (**Table S3**). It must be noted, however, that we observed significantly decreased body weights in male and female *Cln6^{necl}* mice at this time point (**Fig. S3**). Since SUV is negatively correlated with body weight, this complicates any comparison of SUV values between groups. These results, obtained at the advanced stage of 13 months of age, suggest that finding significant differences in ¹⁸F-FEPPA uptake at earlier time points may be even more challenging. Taken together, the differences we observed could be indicative of alterations in glucose uptake, brain perfusion, neuronal metabolism, and inflammatory status.

Kinematic Gait Analysis identifies novel motor disturbances in Cln6^{necl} mice.

The profound anatomical and metabolic abnormalities we observed in *Cln6^{necl}* mice would be expected to lead to behavioral disturbances. While motor coordination deficits have been identified in *Cln6^{necl}* mice using crude measures such as rotarod performance (9, 38), an exhaustive analysis of gait parameters that have good human correlates in the clinic has not been conducted. We used kinematic gait analysis (KGA) to examine 97 gait parameters longitudinally in the *Cln6* mutant mice (**Table S4, Fig. S4-S9**). This included a detailed analysis of gait cycle, body and head orientation and positioning, and multiple fore and hind limb parameters. Additionally, we used a PCA based approach to calculate overall gait scores.

Many individual parameters varied between genotypes and time points, but several predominant gait features defined the *Cln6^{necl}* gait. *Cln6^{necl}* mice ambulated with slower overall speed, decreased durations of diagonal gait mode (trotting), increased durations of double support, slower overall speed, lower hind body posture reflected in lower tail base, hip and iliac crest heights and decreased knee and ankle heights, and elevated toe clearance in both fore and hind limbs (**Fig. S4**). Different gait features, which are manifested in sets of highly correlating parameters, can be identified using principal component analysis [PCA; (39)]. PCA is a commonly used technique to reduce the dimensionality of multivariate data sets (40, 41), or more specifically, to determine a few linear combinations of the original variables that can be used to summarize the data set while retaining as much information as possible. Moreover, the use of PCA also enables the inspection and identification of the mutual correlations between the original kinematic parameters. PCA based calculation of overall gait scores revealed profound and progressive changes in *Cln6^{necl}* mice (**Fig. 3**). The overall score is a weighted average of the gait variables using weights from the discriminant vectors, which emphasizes which kinematic parameters are contributing to the overall score (**Fig. 3B**). When analyzing pooled sexes, *Cln6^{necl}* gait scores were significantly different from controls at all time points, culminating in an approximately 12-fold increase at 12 months of age. When analyzing sexes individually, individual sex score in males increased significantly beginning at 6 months of age. In females, the differences was significant only at 12 months of age. Additionally, there was a significant genotype by age interaction in gait scores, supporting differences in gait over time across the two genotypes (**Fig. 3A**). These results demonstrate that *Cln6* mutant mice have profound, progressive gait disturbances, mirroring phenotypes that have been described in human CLN6 disease patients (42, 43).

Contrastive PCA identifies the core progressive symptomatology in Cln6^{necl} mice.

Where other studies or natural history studies have fallen short is that they try to look at each individual parameter in isolation rather than looking at the system as a whole. We performed contrastive PCA (cPCA) in an effort to holistically capture the progressive changes present in *Cln6^{necl}* mice. Our phenotypic analysis identified a number of novel anatomical, metabolic, and behavioral phenotypes associated to the *Cln6* mutant animals. This large volume of data presented an important question: *Is there a core set of phenotypes that strongly correlate with one another and best describe the progressive nature of the Cln6^{necl} disease course?* Identifying such a set of phenotypes would be of great utility in utilizing this model for not only preclinical testing of novel therapies but could have profound clinical value. So instead of looking for ‘a single needle in a haystack,’ we analyzed ‘the whole haystack’ using statistical methods capable of reducing the data without losing any information.

To perform this analysis, we used a recently developed statistical technique, contrastive PCA (cPCA) (44). This procedure identifies a low dimensional structure that is enriched in one genotype over another, thus calculating cPC scores that accentuate differences between genotypes. Our analysis included MRI volumetry from 6 brain regions, DTI from 9 white matter regions, MRS for 19 metabolites in the PFC, FDG-PET from 15 brain regions, and KGA for 97 parameters, longitudinally from both genotypes of mice. First, we calculated 1st level principal components (PCs), three for each modality. This reduced the original 144 variables yielding 15 unique variables (PCs), many of which highlighted progressive changes in *Cln6^{necl}* mice (**Fig. 4**).

Next, we used cPCA to calculate 2nd level cPC scores based on the 1st level PCs (**Fig. 5**). The top cPC score, cPC1, included contributions primarily from MRI, FDG-PET, DTI, and KGA, demonstrating that gait performance was associated with anatomical and metabolic changes in various brain regions (**Fig. 5A**). cPC1 proved to be very effective at characterizing phenotypic progression in *Cln6^{necl}* mice (**Fig. 5B**). The top 5 features (i.e., the five 1st level PCs with highest contribution) in the cPC1 were: 1) MRI PC1 (overall brain volume), 2) KGA PC1 (overall speed + diagonal cadence + overall hip height), 3) FDG PC3 (increase in striatum, central grey matter, and basal forebrain associated with decrease in cerebellum and olfactory bulb.), 4) DTI PC1 (overall level), and 5) DTI PC2 (increase in the body of the corpus callosum and splenium of the corpus callosum, decrease in anterior commissure, internal capsule and cerebral peduncle). Taken together, the decreased cPC1 score in *Cln6* mutant mice can be interpreted as decrease in structural brain volume (MRI PC1) associated with decrease in overall mobility (KGA PC1), and metabolic changes (FDG PC3), and reductions in overall (DTI PC1) and local (DTI PC2) anisotropy. Remarkably, the genotype difference was significant at each of the time points examined for pooled sexes, as well as each sex separately. The second cPC, cPC2, highlighted a much wider variability in *Cln6^{necl}* mice at all time points. The variation in cPC2 is mostly explained by difference between sexes within *Cln6* mutant animals. There was a significant difference between *Cln6^{necl}* male versus *Cln6^{necl}* female at all time points. The variation in cPC2 is mostly explained with MRI PC2 (hippocampus (↑), cerebellum/lateral ventricles (↓)) and MRI PC3 (cerebellum (↓), lateral ventricles (↑))

(Fig. 5A). However, partially due to this variability, differences between genotypes were mostly insignificant (Fig. 5B). Still, cPC1 provides a powerful summary of the *Cln6^{necl}* phenotype starting early in disease, and could be the basis for highly sensitive assays for future therapeutic testing. Thus, the data from this comprehensive analysis could be used for generating a final disease score, given the longitudinal differences between genotypes. Such a score could in turn be used to determine efficacy of potential treatments in clinical trials.

Discussion

Pediatric neurodegenerative disorders are typically diagnosed by a combination of clinical assessment, neuroradiologic imaging, cellular pathology, and genetic testing (45-47). Unfortunately, even with advancements in genomic diagnostics, seldom are children definitively diagnosed following initial clinical assessment, and more typically, numerous misdiagnoses are offered before a correct diagnosis (48). The clinical features of Batten disease, are a combination of cognitive dysfunction, dementia, retinopathy, and seizures (49-52) but can vary depending on the subtype of the disease and the precise genetic mutation the parent has. Common phenotypic features include muscular hypotonia, microcephaly, myoclonus, epilepsy, ataxia, behavioral changes, visual decline, and brain atrophy (29, 51-55). Although there have been reported sex differences in Batten disease patients, scientists have historically focused on one sex or mixed sexes for behavioral and pathological changes. By separating and tracking individual sexes, this study provides an innovative way of monitoring these animals over time, strengthening the translational utility. Our findings reinforce that the *Cln6^{necl}* model recapitulates many aspects of the human disease course, including the progressive nature, of CLN6 disease. We show that *Cln6^{necl}* mice have profound and progressive changes in brain anatomy and metabolism, and that these changes correlate strongly with abnormalities in gait parameters. cPC1, which encapsulates the changes that appeared most consistently and with the greatest magnitude, shows very large and increasing differences between wild type and *Cln6^{necl}* mice from 6-12 months of age. In addition to providing insights into the pathological manifestations of *Cln6* deficiency, this work suggests a number of clinical assessments that may be most useful in assessing CLN6 patients. Although our genetically identical mice differ in many important ways from a more heterogeneous population of human patients, the beauty of this system is that it isn't reliant on one metric to produce the score of disease state, and can still detect progressive changes in the presence of between-individual variance.

In Batten disease patients, general brain structure changes include cerebral and cerebellar atrophy, callosal thinning, enlarged ventricular space, white matter maturation, and thalamic density, which may appear abnormal before any clinical symptoms appear (29, 53, 55-63). White matter and basal ganglia of the thalami display significantly decreased signal intensity T2-weighted MR images in addition to the increased signal of the periventricular matter (56, 58, 60, 64, 65). Single photon emission computed tomography studies show hypoperfusion in cerebral and cerebellar cortices, most prominent in anterior frontal, posterior temporoparietal and occipital cortices, and abnormal lesions can be detected before structural abnormalities appear (66-69). MRS has shown reductions in N-acetyl aspartate (NAA), glutamine + glutamate + GABA (Glx), creatine (Cr) and choline (Cho) compounds, and elevation of lactate, lipids, and myoinositol (mIns) (53, 60, 61, 70, 71). Additionally, PET imaging show dysfunction of nigrostriatal dopaminergic neurons (reduced [¹⁸F]fluorodopa uptake) (72), reduced metabolism beginning in the calcarine area followed by a widespread decrease throughout the cortex and thalamus (decreased glucose utilization in FDG-PET) (73), and impaired striatal neuronal function (reduced striatal dopamine D1) (74).

The functional imaging modalities employed here revealed significant changes in the diseased mice that also correlate with similar changes reported for Batten disease patients. The *Cln6^{necl}* mice display generalized whole brain atrophy starting at 6 months of age that rapidly progresses, and a reduction in brain metabolites and metabolism as measured by MRI, MRS and FDG-PET, respectively. Region-specific volumetry changes included decreased volume of the cortex and cerebellum. Additionally, there was an opposite trend between male and female diseased mice for lateral ventricle volume, with males showing an increase in ventricular volume at 3 months that was stabilized through 12 months of age, while females showed a steady decrease in ventricular volume over time. These results may be in part due the general decrease in brain volume for both sexes. MRS identified a severe reduction in NAA at 9 – 12 months for both males and females. FDG-PET revealed highly reduced glucose metabolism in all brain regions at 12 months of age. Diffusion tensor MRI and fractional anisotropy showed that brain changes in *Cln6^{necl}* mice involve not only grey matter, but white matter as well. Contrary to many neurodegenerative diseases where corpus callosum changes are often pronounced, deeper white matter structures such as anterior commissure, external and internal capsule seem to be primarily affected in *CLN6^{necl}* mice although corpus callosum changes become evident with disease progression. Decrease of FA is normally attributed to e.g. demyelination, axonal loss/disruption or incoherence due to pathological processes. Unfortunately, supporting NCL related histology-verified DTI research, both clinical and pre-clinical, is still largely lacking. Our data takes important steps in providing observations from animal models of NCL that can be utilized to justify the use of DTI more often in a neuroradiological assessment of Batten disease.

Although motor coordination deficits have been identified in *Cln6^{necl}* mice using behavioral tests such as rotarod performance (9, 38), traditionally, there have been significant inter- and intra-lab variability in animal behavior testing. Variation in behavior results have depended on genetic background of the mouse model, genetic drift, breeding strategies, geographical location of testing facility, variability in behavior protocols implemented, gender of the animal handler, animal diet, and water quality (75, 76). As for differences in behavior testing protocols, different labs implement various training time and number of repeated measures. Fine kinematic gait analysis conducted on 97 unique measurements identified unique movement scores among the *Cln6^{necl}* mice. The overall gait score is based on differences between the wild type and *Cln6^{necl}* groups in all the PC scores. Ultimately, the overall kinematic effects of a

pharmacological agent may be seen in a highly sensitive manner with a wide therapeutic window, which suggests that this tool will be of great value for further preclinical and translational studies in various neurodegenerative disease.

Our results demonstrate the translational power of an exhaustive, multi-factorial characterization of biomarkers in the *Cln6^{ncif}* mouse model of CLN6 disease. Our characterization suggests which clinical tools may be most useful in monitoring patients, and also provides a highly sensitive platform for testing therapies in mice. We focused on two main categories of tools which have direct correlates in the clinic: kinematic gait analysis (KGA) and noninvasive neuroimaging. KGA monitors ambulating mice, capturing a large number of metrics that together describe deviations from normal gait. This method is widely employed in the clinic to objectively describe gait abnormalities in patients. While there are large differences in ambulation mode between bipedal humans and quadrupedal mice, recent developments have demonstrated correlations between parameters of human and mouse gait, and the translational utility of gait analysis in mouse models (25). Similarly, in terms of noninvasive brain imaging, there are many anatomical similarities between the human and murine brain, and studies have shown that noninvasive imaging often detects similar changes in human patients and mouse models of neurodegenerative disease (26).

Furthermore, many researchers have focused on single blood-, saliva-, and cerebrospinal fluid-based biomarkers in mice and large animal models of Batten disease (21-23, 77-80). These focused studies have led us to conclude that no singular target will provide a reliable biomarker of Batten disease. Additionally, one particularly important study analyzed autopsy brains and cerebrospinal fluid (CSF) from deceased Batten disease patients and identified numerous significant changes of potential biomarkers of disease (81). However, this study was conducted on post-mortem brain samples and CSF, which would represent samples that are either impossible to analyze in living patients or invasively acquired. We sought to go beyond simply identifying a single biomarker or group of phenotypes that are present in this mouse model, and to provide a more useful characterization that also identifies which phenotypes correlate most closely with one another, and which phenotypes best demonstrate the progressive nature of the disease. To accomplish this goal, we used cPCA, which is highly effective for identifying the parameters that best define the differences between groups. This analysis is intended to identify cPCs that amplify the differences between healthy and disease subjects, thus increasing the sensitivity to detect changes, positive or negative, in disease progression. Such a metric could have great power for identifying potentially useful therapies in preclinical studies in mice, large animal models, or for quantifying progression or therapeutic benefit in patients, and removes the barrier of looking for a single biomarker of disease by combining multiple biomarkers into one clinical score of disease state/progression.

The strength and novelty of this study stems from utilizing multiple non-invasive functional imaging modalities to longitudinally track and compare wild type and diseased animals over time, and combining the noninvasive imaging, including T2-MRI, DT, MRS, and PET, with KGA in a cPCA to generate a disease score. This score identifies diseased animals and provides a robust and translatable platform for long term monitoring of animal models of disease that can also be applied to large animal models of neurodevelopmental and neurodegenerative diseases as well as clinical patients. The platform we have developed will be widely applicable to the study of a variety of animal models of neurodegenerative disease. In addition to identifying novel phenotypes of these disorders, this combination of neuroimaging, behavior, and statistical analysis should enable the identification of cPCA-based phenotypes that accentuate progressive changes, greatly enhancing the power of these models for preclinical studies. Furthermore, the translational nature of the techniques this platform utilizes may provide important insights for clinicians regarding which noninvasive imaging and behavioral modalities may be most useful in the diagnosis and ongoing assessment of patients with neurodegenerative diseases. Establishing these parameters for patients with neurodegenerative diseases is imperative for future drug screening and utility in human clinical trials. For CLN6 disease patients currently enrolled in the phase I/II clinical trial (ClinicalTrials.gov Identifier: NCT02725580) (82), there is currently no way to conclusively monitor responses to these treatments over time. Having these capabilities in place would allow for quantitative analysis of patient responses. Additionally, in the future these metrics may be combined with existing data from blood- and CSF-based biomarkers to develop a comprehensive panel of noninvasive biomarkers for many neurodegenerative diseases.

Materials and Methods

Study Design

Neuroimaging, gait analysis, and principal component analyses were conducted on aged-matched wildtype and *Cln6* mutant mice (description of animals in Ethics Statement/Animals) to determine a longitudinal biomarker scoring system in a preclinical model of neuropediatric disease. We hypothesized that by looking at various non-invasive disease markers as a system, rather than individually, we could provide a highly sensitive tool that may be translatable to the clinic. Sample size, endpoints, and rules for stopping data collection were determined based on our previously published studies on this model (83). No outliers were removed from any data sets. All animal experiments were performed as specified in the license authorized by the national Animal Experiment Board of Finland and according to the National Institutes of Health (Bethesda, MD, USA) guidelines for the care and use of laboratory animals. Experiments were conducted in an AAALAC accredited laboratory. Animals' care was in accordance with institutional guidelines. 3-13 month, male and female wild type (WT) and homozygous *Cln6*-mutant mice (*Cln6^{ncif}*; JAX stock #003605) on C57BL/6J backgrounds were utilized for all studies, were housed under identical conditions, and all experimenters were blinded to genotype.

Magnetic Resonance Imaging and Spectroscopy

MRI experiments were performed using a horizontal 11.7T magnet with a bore size of 160 mm, equipped with a gradient set capable of maximum gradient strength of 750 mT/m and interfaced to a Bruker Avance III console (Bruker Biospin GmbH, Ettlingen, Germany). A volume coil (Bruker Biospin GmbH, Ettlingen, Germany) was used for transmission and a surface phased array coil for receiving (Rapid Biomedical GmbH, Rimpfing, Germany). Mice were anesthetized using isoflurane, fixed to a head holder and positioned in the magnet bore in a standard orientation relative to gradient coils. Temperature of the animals were monitored and maintained between 36-37°C throughout the experiments. To avoid prolonged anesthesia/study day, MR experiments were performed in two separate scanning sessions; 1) MRI volumetry and localized ¹H-MR spectroscopy from frontal cortex (total duration appr. 45 minutes) and 2) diffusion tensor imaging (DTI, total duration appr. 1 hour).

Structural MRI was performed with a standard Turbo-RARE sequence with TE_{eff} of 34 ms (RARE factor of 8), TR of 3150 ms and 8 averages. Thirty-one 0.45 mm slices were collected with field-of-view of 20x20 mm² and 256x256 matrix (78 microns in-plane resolution). Region of interest analysis was performed in MATLAB (Mathworks Inc., Natick, MA, USA) environment observer blinded for study groups. Whole brain, cortex, striatum, hippocampus, lateral ventricle and cerebellar volumes were analyzed.

For the acquisition of proton MRS data, frontal cortex voxel (2.2x1.6x1.8 mm³, 6.3 μl localized volume) was selected based on structural MR images described above. Automatic 3D gradient echo shimming algorithm was used to adjust B₀ homogeneity in the voxel. The water signal was suppressed using variable power RF pulses with optimized relaxation delays (VAPOR) to obtain B₁ and T₁ insensitivity. A PRESS sequence (TE = 10 ms) combined with outer volume suppression (OVS) was used for the pre-localization. Data were collected by averaging 512 excitations (frequency corrected for each FID) with TR of 2 s, number of points 2048 and spectral width of 5 kHz. Excitation frequency was shifted -2 ppm, to minimize the chemical shift phenomenon within the selected voxel. In addition, a reference spectrum without water suppression (NT=8) was collected from the identical voxel using the same acquisition parameters. Peak areas for resolved metabolites were analyzed using LCModel (Stephen Provencher Inc., Oakville, Canada) using >CRLB 20% as exclusion criterion for individual metabolites within analyzed spectrum.

Diffusion tensor MRI (DTI) was performed using 4-segment EPI sequence with 30 diffusion directions (TE/TR =23.5/4000 ms, b-values 0 and 970 s/mm²). Field-of-view of 12.80 x 10.24 mm² (with saturation slice) was used with matrix of 160 x 128, resulting 80 microns in-plane resolution. Fifteen 0.6 mm slices were acquired with 6 averages. Preprocessing of DTI-data consisted eddy-current correction and brain masking. Diffusion tensor was calculated using FSL (<https://fsl.fmrib.ox.ac.uk/fsl/>) and resulting fractional anisotropy maps were processed with manual ROI-analysis in the MATLAB environment (Mathworks Inc.) for the following anatomical structures; forceps minor of the corpus callosum (fmi), genu of corpus callosum (gcc); body of corpus callosum (bcc); splenium of corpus callosum (scc); external capsule (ec); anterior commissure anterior part (aca); internal capsule (ic); optic tract (opt); cerebral peduncle (cp).

Longitudinal ¹⁸F-FDG and ¹⁸F-FEPPA PET Imaging

The *Cln6^{ncf}* and wild type mice were longitudinally PET scanned at the age of 4, 6, 9 and 12 months. After an overnight fasting, to standardize blood glucose levels, the mice were injected intravenously with a 150 μl bolus of ¹⁸F-FDG in sterile saline, 14.0 ± 1.5 MBq. The mice were anesthetized with isoflurane 20 minutes after the injection and positioned into small animal PET/CT (BioPET/CT, BioScan, USA). Three mice were scanned simultaneously in list mode for 25 minutes, 30 minutes post the ¹⁸F-FDG injection. PET scan was followed by CT scan for anatomical orientation and CT-based attenuation map for image reconstruction. The sinograms were reconstructed with 3D-OSEM, 1 iteration and 25 subsets, with attenuation correction. Image analysis was performed with PMOD software (PMOD Technologies, Switzerland, v.3.7). The PET images were co-registered with mouse brain MRI template and standardized uptake values (SUVs) were calculated on different brain regions.

At the age of 13 months the *Cln6^{ncf}* and wild type mice were anesthetized with isoflurane, cannulated into lateral tail vein and positioned into small animal PET/CT (BioPET/CT, BioScan, USA). Dynamic 90.5 minute PET scan was started and 150 μl of [¹⁸F] FEPPA, 11.4 ± 1.0 MBq, was injected intravenously 30 seconds after the start of the scan. PET scan was followed by CT scan for anatomical orientation and CT-based attenuation map for image reconstruction. The sinograms were reconstructed with 3D-OSEM, 1 iteration and 25 subsets, with attenuation correction. Image analysis was performed with PMOD software (PMOD Technologies, Switzerland, v.3.7). The PET images were co-registered with mouse brain MRI template and standardized uptake values (SUVs) were calculated on different brain regions from last 30 minutes of the PET scan.

Fine motor kinematic analysis

Mice were subjected to kinematic gait analysis test at 6, 9, and 12 months of age, using a Motorater apparatus (TSE-Systems GmbH, Bad Homburg, Germany) designed for the assessment of fine motor skills in rodents. The equipment consists of a brightly illuminated Plexiglas corridor (153 x 5 x 10 cm) under which is situated a high-speed camera. Prior to the test, the mice were shaved under light isoflurane anesthesia, and the essential body points, such as joints and tail, were marked for tracking. The gait performance data was captured using a camera operated 300 frames per second, imaging the gait simultaneously from three different views (underside and both sides). The movement was analyzed from the three views, first using the Simi Motion software (Simi Reality Motion Systems GmbH, Unterschleissheim, Germany). Approximately 5-6 complete strides were analyzed from each mouse. Only strides with continuous ambulatory movement were included in the data. The raw kinematic data thus comprised of the movements of 24 different body points in coordinates related to the ground. Different gait patterns and movements were analyzed using a custom made automated analysis software, resulting 97 distinctive kinematic gait parameters(84) (Fig. S7-S12) such as: general gait pattern parameters (e.g., stride time and stride speed, step width, stance time and swing time during a stride, interlimb coordination, etc.), body posture and balance parameters (e.g., toe clearance, iliac crest height, hip height, hind limb pro-, and retraction, tail position, tail

381 movements), and fine motor skills (e.g. swing speed during a stride, jerk metric during swing phase, angle ranges and deviations of
382 distinct joints, vertical and horizontal head movements).

383 **Principal Component Analysis (PCA)**

384 PCA is a linear transformation based on principal component coefficients and eigenvectors. The transformed, new,
385 uncorrelated variables are called the principal components (PC). The first PC corresponds to such linear combination of data which
386 has the largest possible variance. The second PC has again the largest possible variance of what is left when the proportion of the first
387 PC is discarded, and so on for the rest of the PCs. The total number of PCs was selected using Kaiser's rule, i.e., only those PCs were
388 retained which explain more (variance) than one normalized original variable. The eigenvectors also reveal information about the
389 internal structure of the data, i.e., mutually correlated parameters. Each PC score is emphasized by different combination of mutually
390 correlated original variables. So, each PC is a linear combination of original variables, such that some variables are emphasized in one
391 PC and some other variables in another. Variables which are emphasized in a PC are mutually correlated. On the other hand, the PCs
392 themselves are totally uncorrelated.

393 The Overall Gait Score is based on differences between the wild type and the *Clng^{ncf}* groups in all the PC scores. Thus, the
394 purpose of that score is to identify a combination of original variables, a "fingerprint", which characterizes the disease model in the
395 best possible way and differentiates the two groups. After the "fingerprint", or discriminant direction vector, has been constructed, the
396 overall gait analysis scores are obtained by projecting the (normalized) parameter data of each individual mouse onto the discriminant
397 direction vector. The average wild type group individual has always score equal to zero, and roughly half of the controls have always
398 negative score, reflecting that their overall gait performance is in the opposite direction than the performance of the disease model
399 phenotype. Moreover, the average disease model phenotype has always a positive score value, and the magnitude of that value
400 corresponds to magnitude of phenotype specific deviations in an overall gait pattern.

401 The cPCA is based on PCA of two datasets, X and Y, where X (target) may consist of data of different genotypes, ages,
402 treatments and sexes, and Y (background) consists of control group data, not including variation due to genotype or disease model.
403 The aim in cPCA is to create a subset combination of original parameters, which simultaneously 1) maximizes variance in X
404 (interesting *and* "universal" features) and 2) minimizes variance in Y ("universal" features only). In other words, the cPCA is used to
405 discover the combination of those interesting variables, which all together add contrast between the background and the target, i.e.,
406 genotype specific variables.

407 **Statistical Analysis**

408 Individual tests were run in Graphpad Prism (Ver 7.04). In general, an ordinary two-way ANOVA was used at each time
409 point, using genotype and brain region/metabolite as main factors. An uncorrected Fisher's LSD test was used to determine statistical
410 significance in individual brain regions/metabolites across genotypes. Specific statistical tests and sample size are described in the
411 figure legends. Raw data and complete data tables with exact p-values are available from the authors upon reasonable request. Graphs
412 as presented as Mean +/- SEM, *p<0.05, **p<0.01, ***p<0.001, ****p<0.0001. PCA was performed and cPCA was implemented and
413 performed in R according to Abid et al. (44): A language and environment for statistical computing (Version 3.5.0, R Foundation for
414 Statistical Computing, Vienna, Austria).

416 **Supplementary Materials**

417 Figure S1: Longitudinal brain structural changes in sex separated data

418 Figure S2: Longitudinal fractional anisotropy changes in sex separated data

419 Figure S3: Body weight analysis at 13 months

420 Figure S4: Spatiotemporal kinematic parameters

421 Figure S5: Interlimb coordination parameters

422 Figure S6: Kinematic parameters describing body posture, toe clearance, hind limb protraction and retraction, nose height and head
423 rotation

424 Figure S7: Kinematic parameters describing limb trajectory profiles and excess movements during swing phase of gait

425 Figure S8: Kinematic parameters describing tail tip movements

426 Figure S9: Hip, knee and ankle angles

427 Table S1: MRI volumetry values

428 Table S2: Diffusion tensor imaging: fractional anisotropy values

429 Table S3: FEPPA-PET: ¹⁸F-FEPPA standard uptake values

430 Table S4: Kinematic gait parameters and definitions

432

References and Notes:

- 433 1. N. C. f. A. T. S. NIH. (2017), vol. 2018.
- 434 2. P. Santavuori, L. Lauronen, K. Kirveskari, L. Aberg, K. Sainio, Neuronal ceroid lipofuscinoses in childhood. *Suppl Clin*
- 435 *Neurophysiol* **53**, 443-451 (2000).
- 436 3. J. A. Rider, D. L. Rider, Batten disease: past, present, and future. *Am J Med Genet Suppl* **5**, 21-26 (1988).
- 437 4. A. Schulz, A. Simonati, M. Laine, R. Williams, A. Kohlschütter, M. Nickel, OP48 – 2893: The DEM-CHILD NCL
- 438 Patient Database: A tool for the evaluation of therapies in neuronal ceroid lipofuscinoses (NCL). *European Journal of*
- 439 *Paediatric Neurology* **19**, S16 (2015)10.1016/S1090-3798(15)30049-0).
- 440 5. H. R. Adams, J. W. Mink, G. University of Rochester Batten Center Study, Neurobehavioral features and natural history of
- 441 juvenile neuronal ceroid lipofuscinosis (Batten disease). *Journal of child neurology* **28**, 1128-1136
- 442 (2013)10.1177/0883073813494813).
- 443 6. F. J. Marshall, E. A. de Blicke, J. W. Mink, L. Dure, H. Adams, S. Messing, P. G. Rothberg, E. Levy, T. McDonough, J.
- 444 DeYoung, M. Wang, D. Ramirez-Montealegre, J. M. Kwon, D. A. Pearce, A clinical rating scale for Batten disease: reliable
- 445 and relevant for clinical trials. *Neurology* **65**, 275-279 (2005); published online EpubJul 26
- 446 (10.1212/01.wnl.0000169019.41332.8a).
- 447 7. R. Steinfeld, P. Heim, H. von Gregory, K. Meyer, K. Ullrich, H. H. Goebel, A. Kohlschutter, Late infantile neuronal ceroid
- 448 lipofuscinosis: quantitative description of the clinical course in patients with CLN2 mutations. *American journal of medical*
- 449 *genetics* **112**, 347-354 (2002); published online EpubNov 1 (10.1002/ajmg.10660).
- 450 8. S. Worgall, M. V. Kekatpure, L. Heier, D. Ballon, J. P. Dyke, D. Shungu, X. Mao, B. Kosofsky, M. G. Kaplitt, M. M.
- 451 Souweidane, D. Sondhi, N. R. Hackett, C. Hollmann, R. G. Crystal, Neurological deterioration in late infantile neuronal
- 452 ceroid lipofuscinosis. *Neurology* **69**, 521 (2007).
- 453 9. J. P. Morgan, H. Magee, A. Wong, T. Nelson, B. Koch, J. D. Cooper, J. M. Weimer, A murine model of variant late infantile
- 454 ceroid lipofuscinosis recapitulates behavioral and pathological phenotypes of human disease. *PloS one* **8**, e78694
- 455 (2013)10.1371/journal.pone.0078694).
- 456 10. R. T. Bronson, L. R. Donahue, K. R. Johnson, A. Tanner, P. W. Lane, J. R. Faust, Neuronal ceroid lipofuscinosis (nclf), a
- 457 new disorder of the mouse linked to chromosome 9. *American journal of medical genetics* **77**, 289-297 (1998); published
- 458 online EpubMay 26 (
- 459 11. M. Thelen, M. Damme, M. Schweizer, C. Hagel, A. M. Wong, J. D. Cooper, T. Braulke, G. Galliciotti, Disruption of the
- 460 autophagy-lysosome pathway is involved in neuropathology of the nclf mouse model of neuronal ceroid lipofuscinosis. *PloS*
- 461 *one* **7**, e35493 (2012)10.1371/journal.pone.0035493).
- 462 12. C. Kielar, T. M. Wishart, A. Palmer, S. Dihanich, A. M. Wong, S. L. Macauley, C. H. Chan, M. S. Sands, D. A. Pearce, J. D.
- 463 Cooper, T. H. Gillingwater, Molecular correlates of axonal and synaptic pathology in mouse models of Batten disease.
- 464 *Human molecular genetics* **18**, 4066-4080 (2009); published online EpubNov 1 (10.1093/hmg/ddp355).
- 465 13. M. J. Oswald, D. N. Palmer, G. W. Kay, K. J. Barwell, J. D. Cooper, Location and connectivity determine GABAergic
- 466 interneuron survival in the brains of South Hampshire sheep with CLN6 neuronal ceroid lipofuscinosis. *Neurobiol Dis* **32**,
- 467 50-65 (2008); published online EpubOct (10.1016/j.nbd.2008.06.004).
- 468 14. J. D. Cooper, C. Russell, H. M. Mitchison, Progress towards understanding disease mechanisms in small vertebrate models of
- 469 neuronal ceroid lipofuscinosis. *Biochimica et biophysica acta* **1762**, 873-889 (2006); published online EpubOct
- 470 (10.1016/j.bbadis.2006.08.002).
- 471 15. G. W. Kay, D. N. Palmer, P. Rezaie, J. D. Cooper, Activation of non-neuronal cells within the prenatal developing brain of
- 472 sheep with neuronal ceroid lipofuscinosis. *Brain pathology (Zurich, Switzerland)* **16**, 110-116 (2006); published online
- 473 EpubApr (10.1111/j.1750-3639.2006.00002.x).
- 474 16. M. J. Oswald, D. N. Palmer, G. W. Kay, S. J. Shemilt, P. Rezaie, J. D. Cooper, Glial activation spreads from specific cerebral
- 475 foci and precedes neurodegeneration in presymptomatic ovine neuronal ceroid lipofuscinosis (CLN6). *Neurobiol Dis* **20**, 49-
- 476 63 (2005); published online EpubOct (10.1016/j.nbd.2005.01.025).
- 477 17. J. M. Weimer, A. W. Custer, J. W. Benedict, N. A. Alexander, E. Kingsley, H. J. Federoff, J. D. Cooper, D. A. Pearce, Visual
- 478 deficits in a mouse model of Batten disease are the result of optic nerve degeneration and loss of dorsal lateral geniculate
- 479 thalamic neurons. *Neurobiol Dis* **22**, 284-293 (2006); published online EpubMay (10.1016/j.nbd.2005.11.008).
- 480 18. J. M. Weimer, J. W. Benedict, A. L. Getty, C. C. Pontikis, M. J. Lim, J. D. Cooper, D. A. Pearce, Cerebellar defects in a
- 481 mouse model of juvenile neuronal ceroid lipofuscinosis. *Brain research* **1266**, 93-107 (2009); published online EpubApr 17
- 482 (10.1016/j.brainres.2009.02.009).
- 483 19. T. G. Kuhl, S. Dihanich, A. M. Wong, J. D. Cooper, Regional brain atrophy in mouse models of neuronal ceroid
- 484 lipofuscinosis: a new rostrocaudal perspective. *Journal of child neurology* **28**, 1117-1122 (2013); published online EpubSep
- 485 (10.1177/0883073813494479).
- 486 20. L. Parviainen, S. Dihanich, G. W. Anderson, A. M. Wong, H. R. Brooks, R. Abeti, P. Rezaie, G. Lalli, S. Pope, S. J. Heales,
- 487 H. M. Mitchison, B. P. Williams, J. D. Cooper, Glial cells are functionally impaired in juvenile neuronal ceroid lipofuscinosis
- 488 and detrimental to neurons. *Acta neuropathologica communications* **5**, 74 (2017); published online EpubOct 17
- 489 (10.1186/s40478-017-0476-y).
- 490 21. S. Chattopadhyay, M. Ito, J. D. Cooper, A. I. Brooks, T. M. Curran, J. M. Powers, D. A. Pearce, An autoantibody inhibitory
- 491 to glutamic acid decarboxylase in the neurodegenerative disorder Batten disease. *Human molecular genetics* **11**, 1421-1431
- 492 (2002); published online EpubJun 1 (

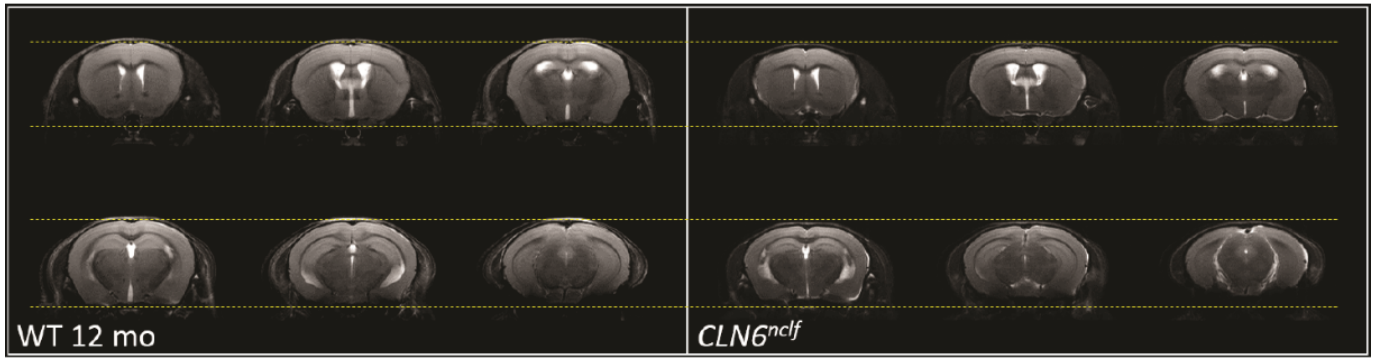
- 493 22. S. Chattopadhyay, E. Kriscenski-Perry, D. A. Wenger, D. A. Pearce, An autoantibody to GAD65 in sera of patients with
494 juvenile neuronal ceroid lipofuscinoses. *Neurology* **59**, 1816-1817 (2002); published online EpubDec 10 (
495 23. S. L. Hersrud, R. D. Geraets, K. L. Weber, C. H. Chan, D. A. Pearce, Plasma biomarkers for neuronal ceroid lipofuscinosis.
496 *The FEBS journal* **283**, 459-471 (2016); published online EpubFeb (10.1111/febs.13593).
497 24. D. Timm, J. T. Cain, R. D. Geraets, K. A. White, S. Y. Koh, T. Kielian, D. A. Pearce, M. L. Hastings, J. M. Weimer,
498 Searching for novel biomarkers using a mouse model of CLN3-Batten disease. **13**, e0201470
499 (2018)10.1371/journal.pone.0201470).
500 25. L. Broom, B. A. Ellison, A. Worley, L. Wagenaar, E. Sorberg, C. Ashton, D. A. Bennett, A. S. Buchman, C. B. Saper, L. C.
501 Shih, J. M. Hausdorff, V. G. VanderHorst, A translational approach to capture gait signatures of neurological disorders in
502 mice and humans. *Sci Rep* **7**, 3225 (2017); published online EpubJun 12 (10.1038/s41598-017-03336-1).
503 26. Y. Waerzeggers, P. Monfared, T. Viel, A. Winkeler, A. H. Jacobs, Mouse models in neurological disorders: applications of
504 non-invasive imaging. *Biochimica et biophysica acta* **1802**, 819-839 (2010); published online EpubOct
505 (10.1016/j.bbadis.2010.04.009).
506 27. H. Braak, H. H. Goebel, Loss of pigment-laden stellate cells: a severe alteration of the isocortex in juvenile neuronal ceroid-
507 lipofuscinosis. *Acta Neuropathol (Berl)* **42**, 53-57 (1978); published online EpubApr 26 (
508 28. J. D. Cooper, The neuronal ceroid lipofuscinoses: the same, but different? *Biochem Soc Trans* **38**, 1448-1452 (2010);
509 published online EpubDec (10.1042/BST0381448).
510 29. J. Radke, W. Stenzel, H. H. Goebel, Human NCL Neuropathology. *Biochimica et biophysica acta* **1852**, 2262-2266 (2015);
511 published online EpubOct (10.1016/j.bbadis.2015.05.007).
512 30. L. J. O'Donnell, C. F. Westin, An introduction to diffusion tensor image analysis. *Neurosurg Clin N Am* **22**, 185-196, viii
513 (2011); published online EpubApr (10.1016/j.nec.2010.12.004).
514 31. M. F. Beal, Aging, energy, and oxidative stress in neurodegenerative diseases. *Annals of neurology* **38**, 357-366 (1995);
515 published online EpubSep (10.1002/ana.410380304).
516 32. M. F. Beal, B. T. Hyman, W. Koroshetz, Do defects in mitochondrial energy metabolism underlie the pathology of
517 neurodegenerative diseases? *Trends in neurosciences* **16**, 125-131 (1993); published online EpubApr (
518 33. R. M. Salek, M. R. Pears, J. D. Cooper, H. M. Mitchison, D. A. Pearce, R. J. Mortishire-Smith, J. L. Griffin, A metabolomic
519 comparison of mouse models of the Neuronal Ceroid Lipofuscinoses. *Journal of biomolecular NMR* **49**, 175-184
520 (2011)10.1007/s10858-011-9491-7).
521 34. J. R. Moffett, B. Ross, P. Arun, C. N. Madhavarao, A. M. Namboodiri, N-Acetylaspartate in the CNS: from neurodiagnostics
522 to neurobiology. *Prog Neurobiol* **81**, 89-131 (2007); published online EpubFeb (10.1016/j.pneurobio.2006.12.003).
523 35. X. Zhu, N. Schuff, J. Kornak, B. Soher, K. Yaffe, J. H. Kramer, F. Ezekiel, B. L. Miller, W. J. Jagust, M. W. Weiner, Effects
524 of Alzheimer disease on fronto-parietal brain N-acetyl aspartate and myo-inositol using magnetic resonance spectroscopic
525 imaging. *Alzheimer Dis Assoc Disord* **20**, 77-85 (2006); published online EpubApr-Jun
526 (10.1097/01.wad.0000213809.12553.fc).
527 36. R. Verma, T. P. Raut, N. Tiwari, K. P. Malhotra, N. Hussain, H. S. Malhotra, Late infantile neuronal ceroid lipofuscinosis: A
528 case report with review of literature. *Ann Indian Acad Neurol* **16**, 282-285 (2013); published online EpubApr (10.4103/0972-
529 2327.112500).
530 37. M. K. Chen, T. R. Guilarte, Translocator protein 18 kDa (TSPO): molecular sensor of brain injury and repair. *Pharmacol*
531 *Ther* **118**, 1-17 (2008); published online EpubApr (10.1016/j.pharmthera.2007.12.004).
532 38. K. M. Kanninen, A. Grubman, A. Caragounis, C. Duncan, S. J. Parker, G. E. Lidgerwood, I. Volitakis, G. Ganio, P. J.
533 Crouch, A. R. White, Altered biometal homeostasis is associated with CLN6 mRNA loss in mouse neuronal ceroid
534 lipofuscinosis. *Biol Open* **2**, 635-646 (2013); published online EpubJun 15 (10.1242/bio.20134804).
535 39. L. M. Schutte, U. Narayanan, J. L. Stout, P. Selber, J. R. Gage, M. H. Schwartz, An index for quantifying deviations from
536 normal gait. *Gait & posture* **11**, 25-31 (2000); published online EpubFeb (
537 40. I. Jolliffe, *Principal Component Analysis*. (Springer-Verlag New York, Inc., New York, ed. 2nd, 2002).
538 41. A. Hervé, W. L. J., Principal component analysis. *Wiley Interdisciplinary Reviews: Computational Statistics* **2**, 433-459
539 (2010)doi:10.1002/wics.101).
540 42. J. Damasio, R. Taipa, M. Melo-Pires, A. Guimaraes, K. P. Bhatia, M. Santos, I. Carrilho, Freezing of gait--first motor
541 manifestation in late infantile variant neuronal ceroid lipofuscinosis. *Parkinsonism Relat Disord* **20**, 243-244 (2014);
542 published online EpubFeb (10.1016/j.parkreldis.2013.10.015).
543 43. R. Guerreiro, J. T. Bras, M. Vieira, V. Warriar, S. Agrawal, H. Stewart, G. Anderson, S. E. Mole, CLN6 disease caused by
544 the same mutation originating in Pakistan has varying pathology. *Eur J Paediatr Neurol* **17**, 657-660 (2013); published
545 online EpubNov (10.1016/j.ejpn.2013.04.011).
546 44. A. Abid, M. J. Zhang, V. K. Bagaria, J. Zou, Exploring patterns enriched in a dataset with contrastive principal component
547 analysis. *Nature communications* **9**, 2134 (2018); published online EpubMay 30 (10.1038/s41467-018-04608-8).
548 45. R. Kohan, I. A. Cismondi, R. D. Kremer, V. J. Muller, N. Guelbert, V. T. Anzolini, M. J. Fietz, A. M. Ramirez, I. N. Halac,
549 An integrated strategy for the diagnosis of neuronal ceroid lipofuscinosis types 1 (CLN1) and 2 (CLN2) in eleven Latin
550 American patients. *Clinical genetics* **76**, 372-382 (2009); published online EpubOct (10.1111/j.1399-0004.2009.01214.x).
551 46. R. Kohan, F. Pesaola, N. Guelbert, P. Pons, A. M. Oller-Ramirez, G. Rautenberg, A. Becerra, K. Sims, W. Xin, I. A.
552 Cismondi, I. Noher de Halac, The neuronal ceroid lipofuscinoses program: A translational research experience in Argentina.
553 *Biochimica et biophysica acta* **1852**, 2301-2311 (2015); published online EpubOct (10.1016/j.bbadis.2015.05.003).

- 554 47. S. E. Mole, S. L. Cotman, Genetics of the neuronal ceroid lipofuscinoses (Batten disease). *Biochimica et biophysica acta*
555 **1852**, 2237-2241 (2015); published online EpubOct (10.1016/j.bbadis.2015.05.011).
- 556 48. M. Fietz, M. AlSayed, D. Burke, J. Cohen-Pfeffer, J. D. Cooper, L. Dvorakova, R. Giugliani, E. Izzo, H. Jahnova, Z. Lukacs,
557 S. E. Mole, I. Noher de Halac, D. A. Pearce, H. Poupetova, A. Schulz, N. Specchio, W. Xin, N. Miller, Diagnosis of neuronal
558 ceroid lipofuscinosis type 2 (CLN2 disease): Expert recommendations for early detection and laboratory diagnosis.
559 *Molecular genetics and metabolism* **119**, 160-167 (2016); published online EpubSep (10.1016/j.ymgme.2016.07.011).
- 560 49. H. H. Goebel, W. Zeman, H. Pilz, Ultrastructural investigations of peripheral nerves in neuronal ceroid-lipofuscinoses
561 (NCL). *Journal of neurology* **213**, 295-303 (1976); published online EpubOct 4 (
- 562 50. S. Meyer, U. Yilmaz, Y. J. Kim, R. Steinfeld, G. Meyberg-Solomayer, B. Oehl-Jaschkowitz, A. Tzschach, L. Gortner, J. Igel,
563 O. Schofer, Congenital CLN disease in two siblings. *Wiener medizinische Wochenschrift (1946)* **165**, 210-213 (2015);
564 published online EpubMay (10.1007/s10354-015-0359-4).
- 565 51. S. B. Dolisca, M. Mehta, D. A. Pearce, J. W. Mink, B. L. Maria, Batten disease: clinical aspects, molecular mechanisms,
566 translational science, and future directions. *Journal of child neurology* **28**, 1074-1100 (2013); published online EpubSep
567 (10.1177/0883073813493665).
- 568 52. J. W. Mink, E. F. Augustine, H. R. Adams, F. J. Marshall, J. M. Kwon, Classification and natural history of the neuronal
569 ceroid lipofuscinoses. *Journal of child neurology* **28**, 1101-1105 (2013); published online EpubSep
570 (10.1177/0883073813494268).
- 571 53. H. H. Goebel, K. E. Wisniewski, Current state of clinical and morphological features in human NCL. *Brain pathology*
572 (*Zurich, Switzerland*) **14**, 61-69 (2004); published online EpubJan (
- 573 54. P. Santavuori, Neuronal ceroid-lipofuscinoses in childhood. *Brain & development* **10**, 80-83 (1988).
- 574 55. R. E. Williams, L. Aberg, T. Autti, H. H. Goebel, A. Kohlschutter, T. Lonnqvist, Diagnosis of the neuronal ceroid
575 lipofuscinoses: an update. *Biochimica et biophysica acta* **1762**, 865-872 (2006); published online EpubOct
576 (10.1016/j.bbadis.2006.07.001).
- 577 56. S. L. Vanhanen, R. Raininko, P. Santavuori, Early differential diagnosis of infantile neuronal ceroid lipofuscinosis, Rett
578 syndrome, and Krabbe disease by CT and MR. *AJNR. American journal of neuroradiology* **15**, 1443-1453 (1994); published
579 online EpubSep (
- 580 57. P. Santavuori, S. L. Vanhanen, T. Autti, Clinical and neuroradiological diagnostic aspects of neuronal ceroid lipofuscinoses
581 disorders. *Eur J Paediatr Neurol* **5 Suppl A**, 157-161 (2001).
- 582 58. T. Autti, R. Raininko, J. Launes, A. Nuutila, P. Santavuori, Jansky-Bielschowsky variant disease: CT, MRI, and SPECT
583 findings. *Pediatric neurology* **8**, 121-126 (1992); published online EpubMar-Apr (
- 584 59. G. W. Anderson, H. H. Goebel, A. Simonati, Human pathology in NCL. *Biochimica et Biophysica Acta (BBA) - Molecular*
585 *Basis of Disease* **1832**, 1807-1826 (2013); published online Epub2013/11/01/ (<https://doi.org/10.1016/j.bbadis.2012.11.014>).
- 586 60. S. L. Vanhanen, J. Puranen, T. Autti, R. Raininko, K. Liewendahl, P. Nikkinen, P. Santavuori, P. Suominen, K. Vuori, A. M.
587 Hakkinen, Neuroradiological findings (MRS, MRI, SPECT) in infantile neuronal ceroid-lipofuscinosis (infantile CLN1) at
588 different stages of the disease. *Neuropediatrics* **35**, 27-35 (2004); published online EpubFeb (10.1055/s-2004-815788).
- 589 61. E. H. Baker, S. W. Levin, Z. Zhang, A. B. Mukherjee, MRI Brain Volume Measurements in Infantile Neuronal Ceroid
590 Lipofuscinosis. *AJNR. American journal of neuroradiology* **38**, 376-382 (2017); published online EpubFeb
591 (10.3174/ajnr.A4978).
- 592 62. L. Lauronen, P. B. Munroe, I. Jarvela, T. Autti, H. M. Mitchison, A. M. O'Rawe, R. M. Gardiner, S. E. Mole, J. Puranen, A.
593 M. Hakkinen, E. Kirveskari, P. Santavuori, Delayed classic and protracted phenotypes of compound heterozygous juvenile
594 neuronal ceroid lipofuscinosis. *Neurology* **52**, 360-365 (1999); published online EpubJan 15 (
- 595 63. J. Munasinghe, Z. Zhang, E. Kong, A. Heffer, A. B. Mukherjee, Evaluation of neurodegeneration in a mouse model of
596 infantile batten disease by magnetic resonance imaging and magnetic resonance spectroscopy. *Neuro-degenerative diseases*
597 **9**, 159-169 (2012)10.1159/000334838).
- 598 64. T. Autti, R. Raininko, S. L. Vanhanen, P. Santavuori, Magnetic resonance techniques in neuronal ceroid lipofuscinoses and
599 some other lysosomal diseases affecting the brain. *Current opinion in neurology* **10**, 519-524 (1997); published online
600 EpubDec (
- 601 65. V. Holmberg, L. Lauronen, T. Autti, P. Santavuori, M. Savukoski, P. Uvebrant, I. Hofman, L. Peltonen, I. Jarvela,
602 Phenotype-genotype correlation in eight patients with Finnish variant late infantile NCL (CLN5). *Neurology* **55**, 579-581
603 (2000); published online EpubAug 22 (
- 604 66. E. Sayit, I. Yorulmaz, R. Bekis, G. Kaya, F. G. Gumuser, E. Dirik, H. Durak, Comparison of brain perfusion SPECT and
605 MRI findings in children with neuronal ceroid-lipofuscinosis and in their families. *Annals of nuclear medicine* **16**, 201-206
606 (2002); published online EpubMay (
- 607 67. K. Liewendahl, S. L. Vanhanen, H. Heiskala, R. Raininko, P. Nikkinen, J. Launes, P. Santavuori, Brain perfusion SPECT
608 abnormalities in neuronal ceroid lipofuscinoses. *Neuropediatrics* **28**, 71-73 (1997); published online EpubFeb (10.1055/s-
609 2007-973674).
- 610 68. S. L. Vanhanen, K. Liewendahl, R. Raininko, P. Nikkinen, T. Autti, K. Sainio, P. Santavuori, Brain perfusion SPECT in
611 infantile neuronal ceroid-lipofuscinosis (INCL). Comparison with clinical manifestations and MRI findings. *Neuropediatrics*
612 **27**, 76-83 (1996); published online EpubApr (10.1055/s-2007-973753).
- 613 69. J. Launes, H. Heiskala, P. Nikkinen, P. Santavuori, Brain perfusion SPECT in juvenile neuronal ceroid lipofuscinosis.
614 *Neuropediatrics* **27**, 84-87 (1996); published online EpubApr (10.1055/s-2007-973754).

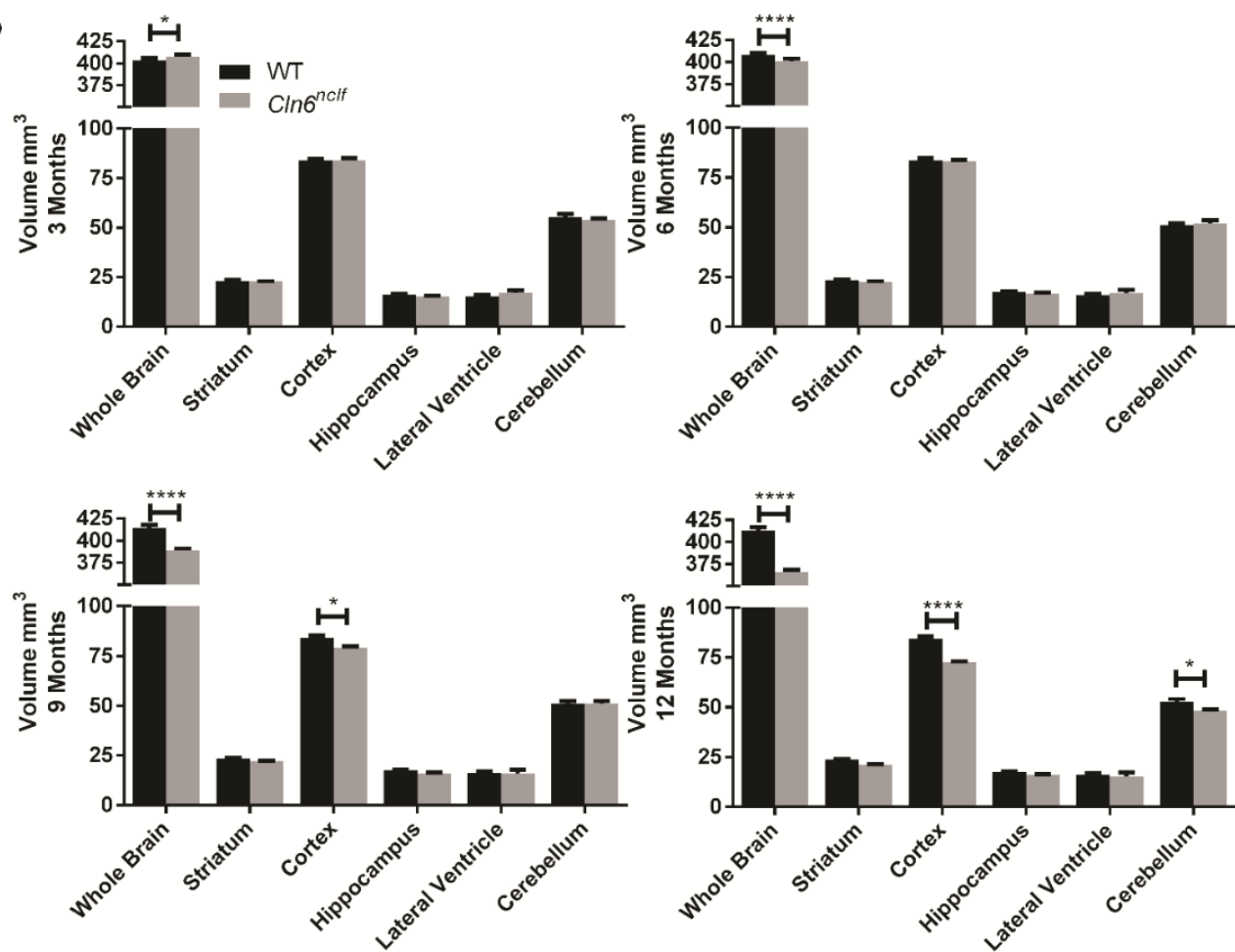
- 615 70. K. Varvagiannis, S. Hanquinet, M. H. Billieux, R. De Luca, P. Rimensberger, M. Lidgren, M. Guipponi, P. Makrythanasis, J.
616 L. Blouin, S. E. Antonarakis, R. Steinfeld, I. Kern, A. Poretti, J. Fluss, S. Fokstuen, Congenital Neuronal Ceroid
617 Lipofuscinosis with a Novel CTSD Gene Mutation: A Rare Cause of Neonatal-Onset Neurodegenerative Disorder.
618 *Neuropediatrics* **49**, 150-153 (2018); published online EpubApr (10.1055/s-0037-1613681).
- 619 71. D. Seitz, W. Grodd, A. Schwab, U. Seeger, U. Klose, T. Nagele, MR imaging and localized proton MR spectroscopy in late
620 infantile neuronal ceroid lipofuscinosis. *AJNR. American journal of neuroradiology* **19**, 1373-1377 (1998); published online
621 EpubAug (
- 622 72. H. M. Ruottinen, J. O. Rinne, M. Haaparanta, O. Solin, J. Bergman, V. J. Oikonen, I. Jarvela, P. Santavuori, [18F]fluorodopa
623 PET shows striatal dopaminergic dysfunction in juvenile neuronal ceroid lipofuscinosis. *Journal of neurology, neurosurgery,
624 and psychiatry* **62**, 622-625 (1997); published online EpubJun (
- 625 73. M. Philippart, C. Messa, H. T. Chugani, Spielmeier-Vogt (Batten, Spielmeier-Sjogren) disease. Distinctive patterns of
626 cerebral glucose utilization. *Brain : a journal of neurology* **117 (Pt 5)**, 1085-1092 (1994); published online EpubOct (
- 627 74. J. O. Rinne, H. M. Ruottinen, K. Nagren, L. E. Aberg, P. Santavuori, Positron emission tomography shows reduced striatal
628 dopamine D1 but not D2 receptors in juvenile neuronal ceroid lipofuscinosis. *Neuropediatrics* **33**, 138-141 (2002); published
629 online EpubJun (10.1055/s-2002-33677).
- 630 75. M. J. Justice, P. Dhillon, Using the mouse to model human disease: increasing validity and reproducibility. *Disease models &
631 mechanisms* **9**, 101-103 (2016); published online EpubFeb (10.1242/dmm.024547).
- 632 76. R. E. Sorge, L. J. Martin, K. A. Isbester, S. G. Sotocinal, S. Rosen, A. H. Tuttle, J. S. Wieskopf, E. L. Acland, A. Dokova, B.
633 Kadoura, P. Leger, J. C. Mapplebeck, M. McPhail, A. Delaney, G. Wigerblad, A. P. Schumann, T. Quinn, J. Frasnelli, C. I.
634 Svensson, W. F. Sternberg, J. S. Mogil, Olfactory exposure to males, including men, causes stress and related analgesia in
635 rodents. *Nature methods* **11**, 629-632 (2014); published online EpubJun (10.1038/nmeth.2935).
- 636 77. J. A. Castaneda, D. A. Pearce, Identification of alpha-fetoprotein as an autoantigen in juvenile Batten disease. *Neurobiol Dis*
637 **29**, 92-102 (2008); published online EpubJan (10.1016/j.nbd.2007.08.007).
- 638 78. A.-H. Lebrun, P. Moll-Khosrawi, S. Pohl, G. Makrypidi, S. Storch, D. Kilian, T. Streichert, B. Otto, S. E. Mole, K. Ullrich,
639 S. Cotman, A. Kohlschütter, T. Bräulke, A. Schulz, Analysis of Potential Biomarkers and Modifier Genes Affecting the
640 Clinical Course of CLN3 Disease. *Molecular Medicine* **17**, 1253-1261 (2011)10.2119/molmed.2010.00241).
- 641 79. G. W. Kay, M. M. Verbeek, J. M. Furlong, M. A. A. P. Willemsen, D. N. Palmer, Neuropeptide changes and neuroactive
642 amino acids in CSF from humans and sheep with neuronal ceroid lipofuscinoses (NCLs, Batten disease). *Neurochemistry
643 International* **55**, 783-788 (2009); published online Epub2009/12/01/ (<https://doi.org/10.1016/j.neuint.2009.07.012>).
- 644 80. D. Timm, J. T. Cain, R. D. Geraets, K. A. White, S. Y. Koh, T. Kielian, D. A. Pearce, M. L. Hastings, J. M. Weimer,
645 Searching for novel biomarkers using a mouse model of CLN3-Batten disease. *PloS one* **13**, e0201470
646 (2018)10.1371/journal.pone.0201470).
- 647 81. D. E. Sleat, A. Tannous, I. Sohar, J. A. Wiseman, H. Zheng, M. Qian, C. Zhao, W. Xin, R. Barone, K. B. Sims, D. F. Moore,
648 P. Lobel, Proteomic Analysis of Brain and Cerebrospinal Fluid from the Three Major Forms of Neuronal Ceroid
649 Lipofuscinosis Reveals Potential Biomarkers. *Journal of proteome research* **16**, 3787-3804
650 (2017)10.1021/acs.jproteome.7b00460).
- 651 82. US National Library of Medicine. *ClinicalTrials.gov*. (2016).
- 652 83. J. P. Morgan, H. Magee, A. Wong, T. Nelson, B. Koch, J. D. Cooper, J. M. Weimer, A murine model of variant late infantile
653 ceroid lipofuscinosis recapitulates behavioral and pathological phenotypes of human disease. *PloS one* **8**, e78694-e78694
654 (2013)10.1371/journal.pone.0078694).
- 655 84. B. Zorner, L. Filli, M. L. Starkey, R. Gonzenbach, H. Kasper, M. Rothlisberger, M. Bolliger, M. E. Schwab, Profiling
656 locomotor recovery: comprehensive quantification of impairments after CNS damage in rodents. *Nature methods* **7**, 701-708
657 (2010); published online EpubSep (
- 658

659 **Acknowledgments: Funding:** This work was supported by funding to JMW NIH R01NS082283 as well as institutional support from
660 Sanford Research and Charles Rivers.. **Author contributions:** K.K.L, A.N and J.M.W conceptualized and designed the
661 studies. D.T. bred and shipped the mice. K.K.L J.R., and T.B. conducted the experiments and generated data. T.B.J., J.J.B.,
662 K.K.L, J.T.C, K.A.W., T.B., J.R. T.B., A.N., and J.M.W. critically analyzed and plotted data. T.B.J and J.J.B wrote the
663 manuscript. T.B.J, J.J.B, K.K.L, J.T.C, K.A.W, T.B, J.R., T.H., M.V., J.T.P., A.N, and J.M.W. reviewed and edited the
664 manuscript. **Competing interests:** The authors declare no competing interests. **Data and materials availability:** All data
665 generated in this study can be found in the paper or supplemental materials or provided upon request.

A



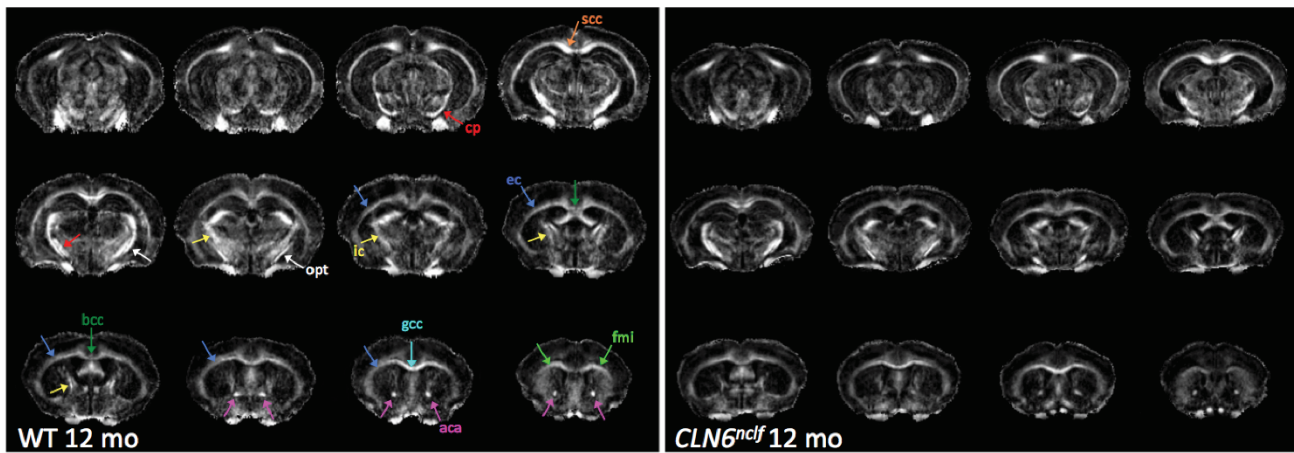
B



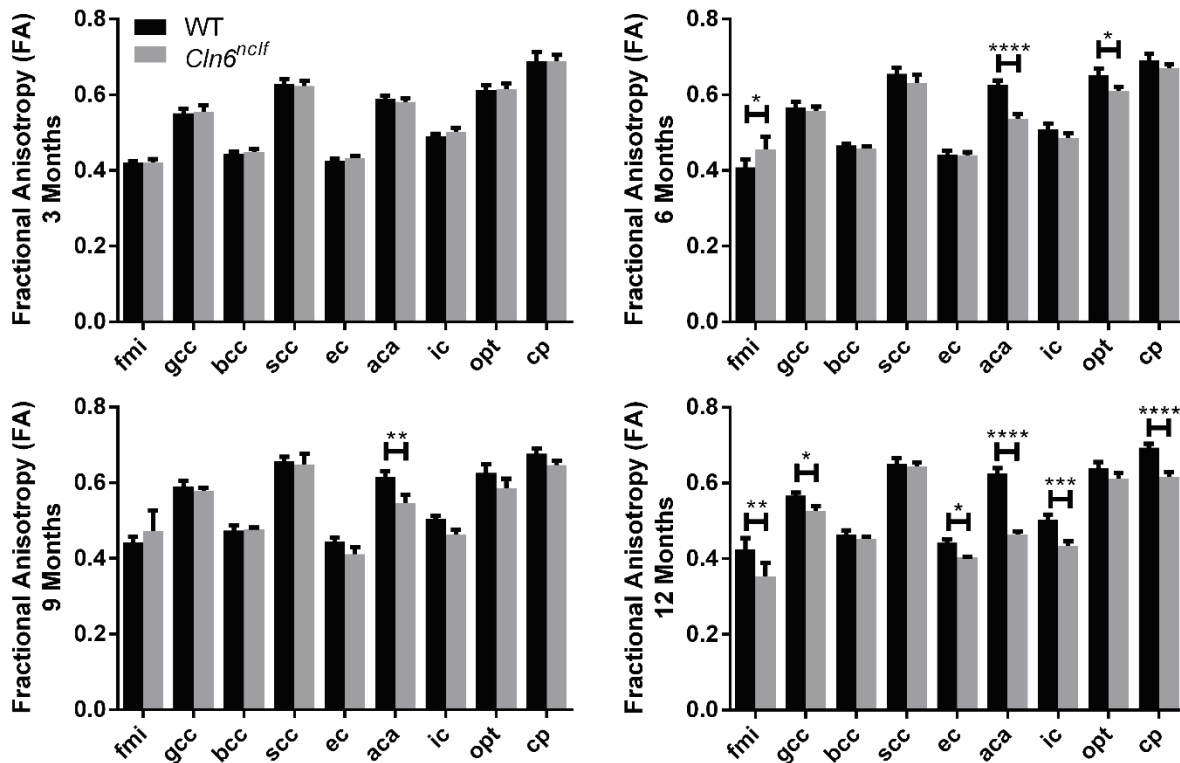
666
667
668
669
670
671
672
673

Fig. 1. 12 month old *Cln6^{nclf}* mice have reduced brain volume in several key regions, as evidenced by MRI volumetry. A) Representative T2 weighted image panels for WT and *Cln6^{nclf}* mice at the age of 12 months. Dashed yellow lines are to guide the eye for evident brain atrophy between the genotypes. B) Longitudinal brain structural changes over 3-12 month observation period. Progressive volume decline is seen in whole brain from 6 to 12 months, cortex volume at 9 and 12 months and cerebellum at 12 months. Data is mean \pm SEM, n = 8 for WT (4 male, 4 female), n = 8 for *Cln6^{nclf}* (4 male, 4 female). Statistical significances: unpaired, two-way ANOVA with Fisher's LSD test. *p < 0.05, ****p < 0.0001.

A



B



674

675 **Fig. 2. Diffusion tensor imaging identifies disrupted white matter architecture beginning at 6 months in *Cln6^{nclf}* mice.** A)
 676 Representative DTI image (fractional anisotropy) panels for WT and *Cln6^{nclf}* mice at the age of 12 months. B) Longitudinal fractional
 677 anisotropy changes over 3-12 month observation period. Progressive white matter declines were detected in the aca beginning at 6
 678 months of age in *Cln6^{nclf}* mice, while various white matter regions showed reduced volumes at 12 months of age. Data is mean \pm SEM,
 679 $n = 8$ for WT (4 male, 4 female), $n = 8$ for *Cln6^{nclf}* (4 male, 4 female). Statistical significances: unpaired, two-way ANOVA with
 680 Fisher's LSD test. * $p < 0.05$, ** $p < 0.01$, *** $p < 0.001$, **** $p < 0.0001$. Abbreviations: fmi – forceps minor of corpus callosum, gcc –
 681 genu of corpus callosum, bcc – body of corpus callosum, scc – splenium of corpus callosum, ec – external capsule, aca – anterior
 682 commissure (anterior part), ic – internal capsule, opt – optic tract, cp – cerebral peduncle.

Table 1. ¹H-MRS: Metabolite Concentration (mmol/kg)

Metabolite	Group	3 months			6 months			9 months			12 months		
		WT	<i>Cln6^{nclf}</i>	p-value	WT	<i>Cln6^{nclf}</i>	p-value	WT	<i>Cln6^{nclf}</i>	p-value	WT	<i>Cln6^{nclf}</i>	p-value
Ala	Female	1.64	1.368	0.2919	1.655	1.863	0.5303	1.285	1.39	0.8316	1.41	0.97	0.2243
	Male	1.2	1.243	0.9181	1.08	1	0.8805	0.9367	1.107	0.6056	1.45	1.11	0.4572
Cr	Female	2.875	2.728	0.568	2.805	2.865	0.8451	2.913	3.283	0.2294	2.945	2.875	0.8025
	Male	3.155	2.775	0.1422	3.138	3.028	0.7203	3.12	3.335	0.4511	3.415	3.273	0.5331
PCr	Female	5.11	4.393	0.0059**	5.048	4.765	0.3583	4.795	4.267	0.0875	4.903	5.005	0.7142
	Male	4.745	4.635	0.6701	4.87	4.415	0.1397	4.543	4.678	0.6359	4.435	4.62	0.4186
GABA	Female	2.503	2.365	0.5945	1.815	2.638	0.008**	2.255	2.42	0.5922	2.358	2.44	0.7682
	Male	2.325	2.853	0.0421*	2.57	2.928	0.2453	2.815	2.353	0.106	2.508	2.268	0.2944
Glc	Female	3.117	2.53	0.0364*	2.623	2.823	0.573	2.643	2.865	0.5471	2.62	2.455	0.5761
	Male	3.66	3.655	0.9845	3.098	3.035	0.8388	2.768	2.948	0.528	2.708	2.533	0.4441
GLN	Female	3.07	2.935	0.6012	3.158	3.395	0.4398	3.24	3.523	0.358	3.42	4.44	0.0004***
	Male	2.788	2.728	0.8162	2.975	3.06	0.782	3.063	3.365	0.2894	2.653	3.438	0.0007***
GLU	Female	11.77	11.41	0.1642	10.85	11.06	0.4945	11.42	11.02	0.2006	11.28	11.45	0.5437
	Male	10.85	11.35	0.0539	11.42	11.63	0.4996	11.67	11.53	0.605	11.44	10.82	0.0078**
GPC	Female	1.168	1.143	0.9229	1.088	1.048	0.8964	1.28	0.9967	0.358	1.12	1.105	0.9594
	Male	1.135	1.005	0.6147	1	1.188	0.5722	1.163	1.113	0.8689	1.063	0.9675	0.6776
PCh	Female	1.253	1.1	0.5549	1.313	1.313	>0.9999	1.23	1.353	0.6888	1.445	1.23	0.4427
	Male	1.145	1.238	0.7202	1.388	1.113	0.3712	1.265	1.16	0.7127	1.298	1.225	0.751
GSH	Female	1.465	1.388	0.7641	1.728	1.498	0.4543	1.505	1.273	0.4521	1.335	1.65	0.2612
	Male	1.723	1.41	0.227	1.678	1.343	0.2762	1.25	1.418	0.557	1.29	1.418	0.577
INS	Female	6.688	5.978	0.0064**	6.578	6.173	0.1883	6.343	6.163	0.5608	6.263	6.13	0.636
	Male	6.24	6.078	0.5293	6.203	5.805	0.1966	5.975	6.09	0.6867	5.825	6.15	0.1562
NAA	Female	7.48	6.715	0.0034**	5.805	6.48	0.029*	7.015	6.47	0.078	7.403	6.475	0.0011**
	Male	6.715	7.095	0.1422	7.253	6.945	0.3174	7.798	6.7	0.0002***	7.52	6.353	<0.0001****

TAU	Female	11.04	9.318	<0.0001****	10.61	10.33	0.3625	10.26	9.73	0.0895	10.53	10.76	0.4015
	Male	11.86	11.09	0.0031**	11.68	10.62	0.0007***	11.16	10.33	0.0041**	11.32	10.63	0.0026**
CHO	Female	2.42	2.243	0.492	2.398	2.36	0.9028	2.515	2.35	0.5922	2.46	2.34	0.6681
	Male	2.28	2.243	0.8845	2.328	2.303	0.9351	2.33	2.273	0.8401	2.363	2.193	0.4572
NAA+NAAG	Female	7.688	7.035	0.0122*	6.568	6.893	0.2908	7.615	6.98	0.0403*	7.893	6.95	0.0009***
	Male	7.265	7.565	0.2461	7.773	7.395	0.22	8.39	7.3	0.0002***	7.908	6.61	<0.0001****
Cr+PCr	Female	7.983	7.123	0.001**	7.853	7.625	0.4593	7.705	7.55	0.6148	7.848	7.88	0.9075
	Male	7.898	7.408	0.0588	8.005	7.44	0.067	7.663	8.013	0.2205	7.85	7.898	0.8353
GLU+GLN	Female	14.84	14.34	0.0539	14.01	14.46	0.144	14.66	14.54	0.7169	14.7	15.9	<0.0001****
	Male	13.64	14.08	0.0913	14.4	14.69	0.3334	14.74	14.89	0.5989	14.09	14.26	0.4507

685

686

687

Red signifies values that have increased and are statistically significant in *Cln6* mice compared to WT mice.

Blue signifies values that have decreased and are statistically significant in *Cln6* mice compared to WT mice.

Table 2. FDG-PET: ¹⁸F-FDG Standard Uptake Values

Brain Region	Group	4 months			6 months			9 months			12 months		
		WT	<i>Cln6^{ncf}</i>	p-value	WT	<i>Cln6^{ncf}</i>	p-value	WT	<i>Cln6^{ncf}</i>	p-value	WT	<i>Cln6^{ncf}</i>	p-value
Amygdala	Female	1.857	1.669	0.4529	2.093	2.045	0.8755	1.778	1.916	0.6507	2.201	1.914	0.1116
	Male	2.041	2.107	0.736	2.258	2.331	0.8146	2.193	2.155	0.9001	2.173	1.792	0.0324*
BFS	Female	2.003	1.881	0.6252	2.46	2.293	0.5864	2.058	2.242	0.5437	2.419	2.17	0.1659
	Male	2.268	2.402	0.498	2.553	2.552	0.9968	2.485	2.427	0.8468	2.383	2.006	0.0338*
Brain Stem	Female	2.36	2.284	0.7623	2.832	2.758	0.8105	2.341	2.439	0.7474	2.847	2.273	0.0015**
	Male	2.856	2.914	0.7685	3.092	3.076	0.96	2.934	2.883	0.8636	2.767	2.245	0.0034**
Central Gray	Female	2.645	2.432	0.3947	3.292	3.051	0.4327	2.731	3.016	0.3482	3.022	2.729	0.1035
	Male	3.073	3.288	0.2752	3.36	3.297	0.8374	3.255	3.271	0.9582	3.01	2.57	0.0135*
Cerebellum	Female	2.489	2.371	0.6366	3.036	2.889	0.6336	2.66	2.701	0.892	2.958	2.388	0.0016**
	Male	2.985	3.158	0.3799	3.208	3.179	0.9247	3.254	3.194	0.841	2.908	2.407	0.0049**
Cortex	Female	2.306	2.117	0.451	2.772	2.541	0.4532	2.193	2.331	0.6499	2.632	2.214	0.0206*
	Male	2.549	2.739	0.3358	2.785	2.756	0.9257	2.653	2.657	0.9894	2.598	2.111	0.0063**
Hippocampus	Female	2.346	2.244	0.6841	3.013	2.777	0.442	2.439	2.713	0.3665	2.805	2.489	0.0789
	Male	2.723	2.939	0.2745	3.057	2.993	0.8374	2.955	2.975	0.9458	2.787	2.299	0.0062**
Hypothalamus	Female	1.874	1.848	0.9179	2.349	2.255	0.7614	1.935	2.148	0.4826	2.357	2.091	0.1394
	Male	2.294	2.291	0.9881	2.554	2.588	0.911	2.437	2.481	0.8829	2.366	2.013	0.047*
Inferior Colliculi	Female	2.45	2.338	0.6545	2.977	2.747	0.455	2.46	2.63	0.5757	2.73	2.362	0.0406*
	Male	2.872	3.03	0.4236	3.14	3.011	0.6788	2.991	2.873	0.6927	2.701	2.284	0.019*
Midbrain	Female	2.441	2.305	0.5867	3.054	2.87	0.5513	2.525	2.765	0.4287	2.87	2.537	0.0643
	Male	2.937	3.107	0.3865	3.205	3.171	0.9139	3.063	3.1	0.9003	2.875	2.415	0.0097**
Olfactory Bulb	Female	2.456	2.19	0.2886	3.156	2.747	0.1846	2.513	2.47	0.8874	2.998	2.135	<0.0001****
	Male	2.871	2.997	0.5224	3.355	3.131	0.4714	3.209	2.877	0.268	3.151	2.121	<0.0001****
Striatum	Female	2.456	2.304	0.5437	3.111	2.868	0.4308	2.553	2.803	0.4102	2.87	2.624	0.1724
	Male	2.796	3.027	0.242	3.091	3.056	0.9122	2.994	2.936	0.8467	2.816	2.352	0.0092**
Superior Colliculi	Female	2.619	2.436	0.4633	3.345	3.053	0.343	2.696	2.969	0.3681	3.03	2.687	0.0569
	Male	3.061	3.251	0.3343	3.377	3.267	0.7236	3.204	3.166	0.8997	2.974	2.48	0.0055**
Thalamus	Female	2.491	2.404	0.728	3.219	2.949	0.3806	2.628	2.853	0.4569	2.968	2.575	0.0291*
	Male	2.966	3.178	0.283	3.232	3.167	0.8328	3.146	3.129	0.9526	2.939	2.391	0.0021**
Whole Brain	Female	2.352	2.206	0.561	2.887	2.687	0.514	2.362	2.502	0.6431	2.765	2.317	0.0131*

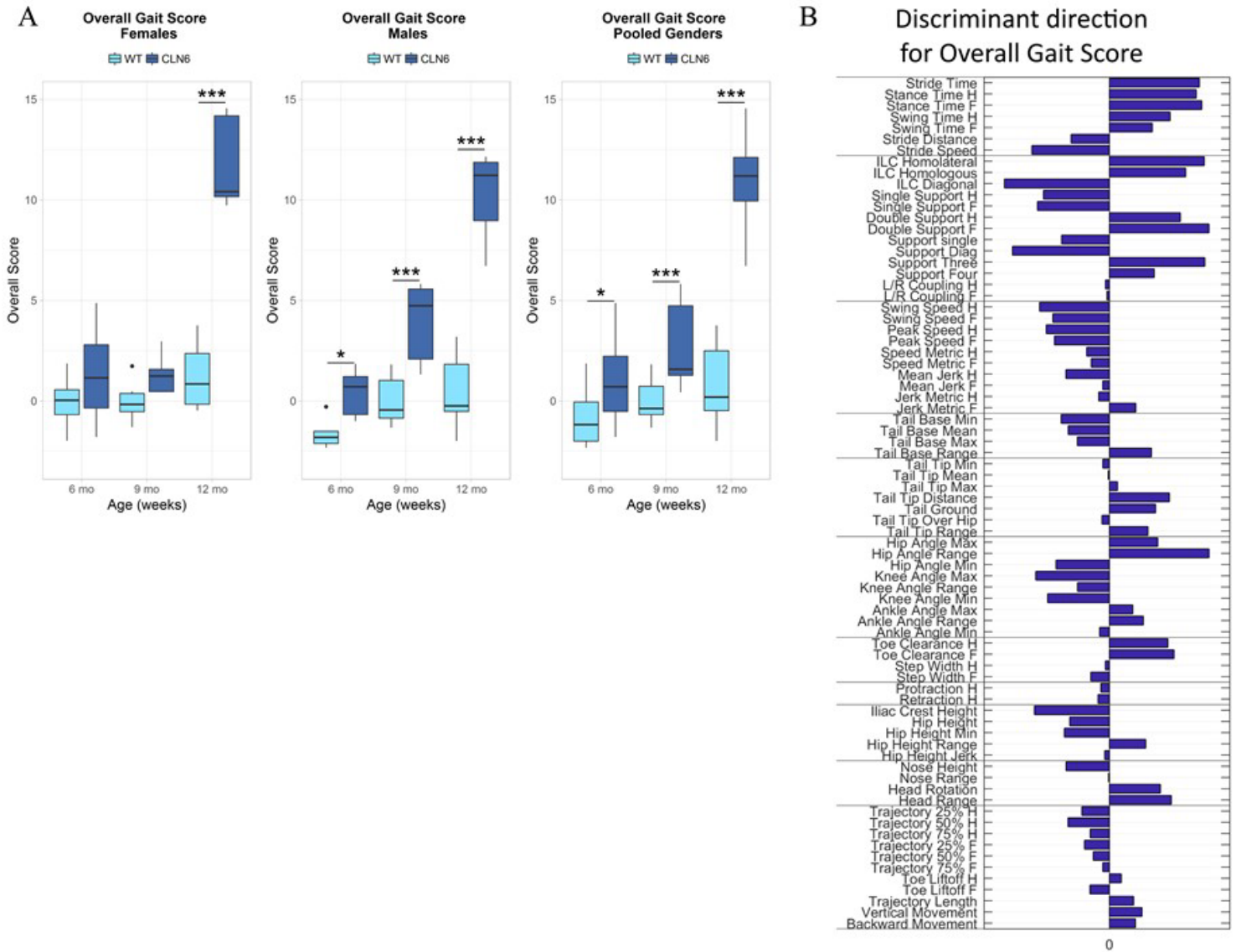
	Male	2.72	2.88	0.4148	2.983	2.942	0.8967	2.88	2.843	0.9011	2.734	2.221	0.0039**
--	------	------	------	--------	-------	-------	--------	------	-------	--------	-------	-------	----------

690

691

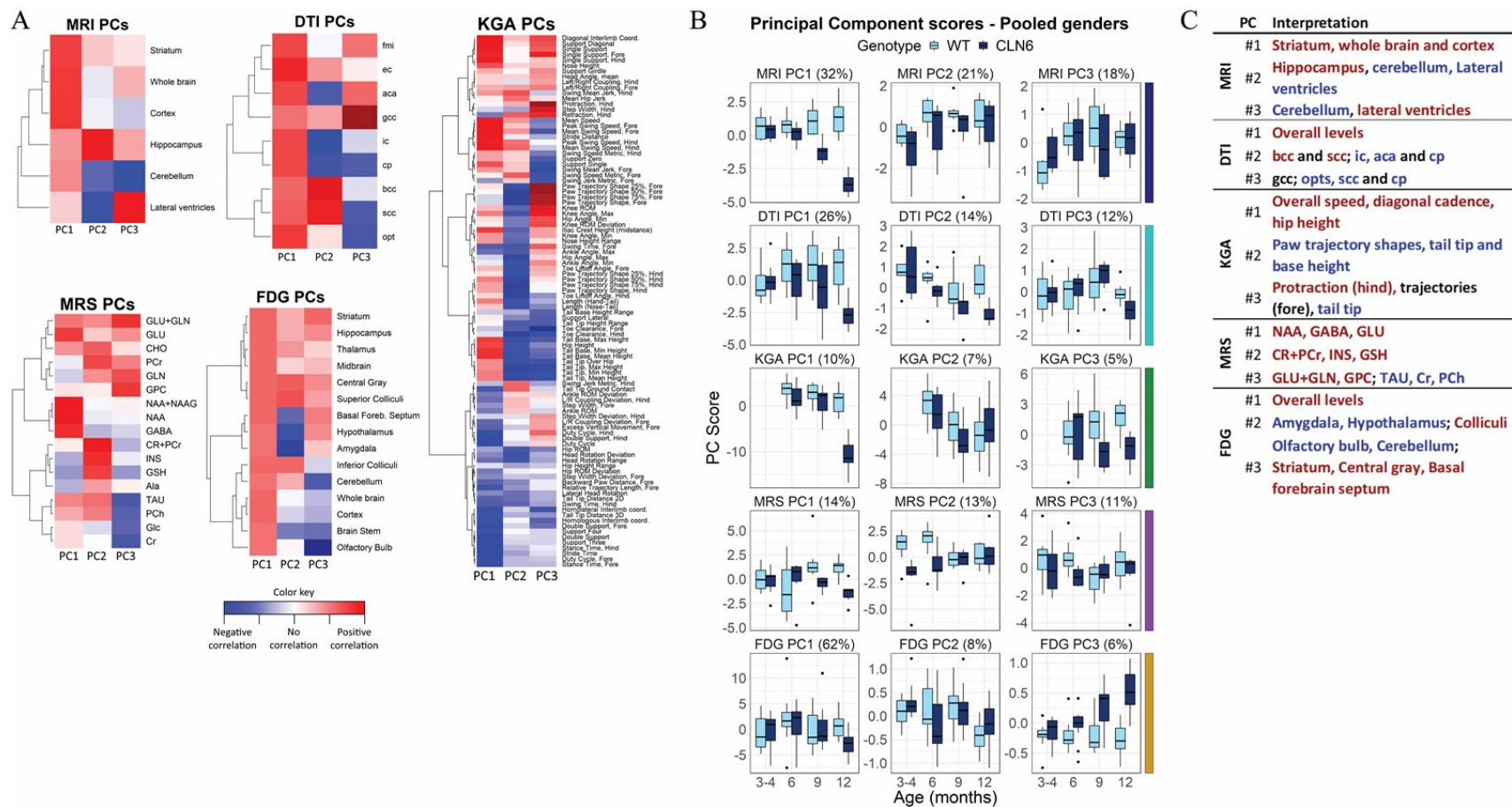
Blue signifies values that have decreased and are statistically significant in *Cln6* mice compared to WT mice.

692



693

694 **Fig. 3. Kinematic gait analysis followed by PCA identifies progressive alterations in gait.** A) The overall score is based on the
 695 principal component score differences between the *Cln6^{nc1f}* and the WT groups in 63 selected kinematic parameters altogether. The
 696 score can be interpreted as “how far away is an individual from the average WT towards the direction of the average *CLN6^{nc1f}*”. The
 697 mean of the WT group score is equal to zero. B) The discriminant direction bar graph illustrates how each kinematic parameter is
 698 weighted in the score. The bar graph also represents an overall kinematic fingerprint of the *Cln6^{nc1f}* model over the three time points:
 699 zero level correspond to average WT. Data is presented as group means +/- SEM. n = 12 for WT (6 male, 6 female), n = 11 for
 700 *CLN6^{nc1f}* (5 male, 6 female). Statistical significances: unpaired t-test * $p < 0.05$, ** $p < 0.01$, *** $p < 0.001$, **** $p < 0.0001$
 701
 702



705 **Fig. 4: Principal component analysis demonstrates how the most influential combinations of non-invasive imaging and gait analysis variables contribute to the**
 706 **progressive changes in the *Clng^{mut}* disease state.** A) Three first principal components of each five modalities, shown as heatmaps, illustrate the identified correlation structure
 707 within each dataset. Strong cell color, red or blue, indicates that the variable has high loading in the corresponding PC. Moreover, a set of variables with high loadings within the
 708 same PC are strongly correlated. The correlation between variables of same color is positive (red or blue), and negative in case of opposite colors (red and blue). For example, in
 709 MRI PC1, volumes of striatum, whole brain and cortex are correlated directly. In MRI PC3, cerebellum and lateral ventricles correlate inversely. B) Interpretations of the principal
 710 components are based on findings which variables are most strongly correlated within each component. C) Phase 1 principal component scores. Data is presented as boxplots. The
 711 percentage numbers indicate variance explained by the corresponding PC.
 712

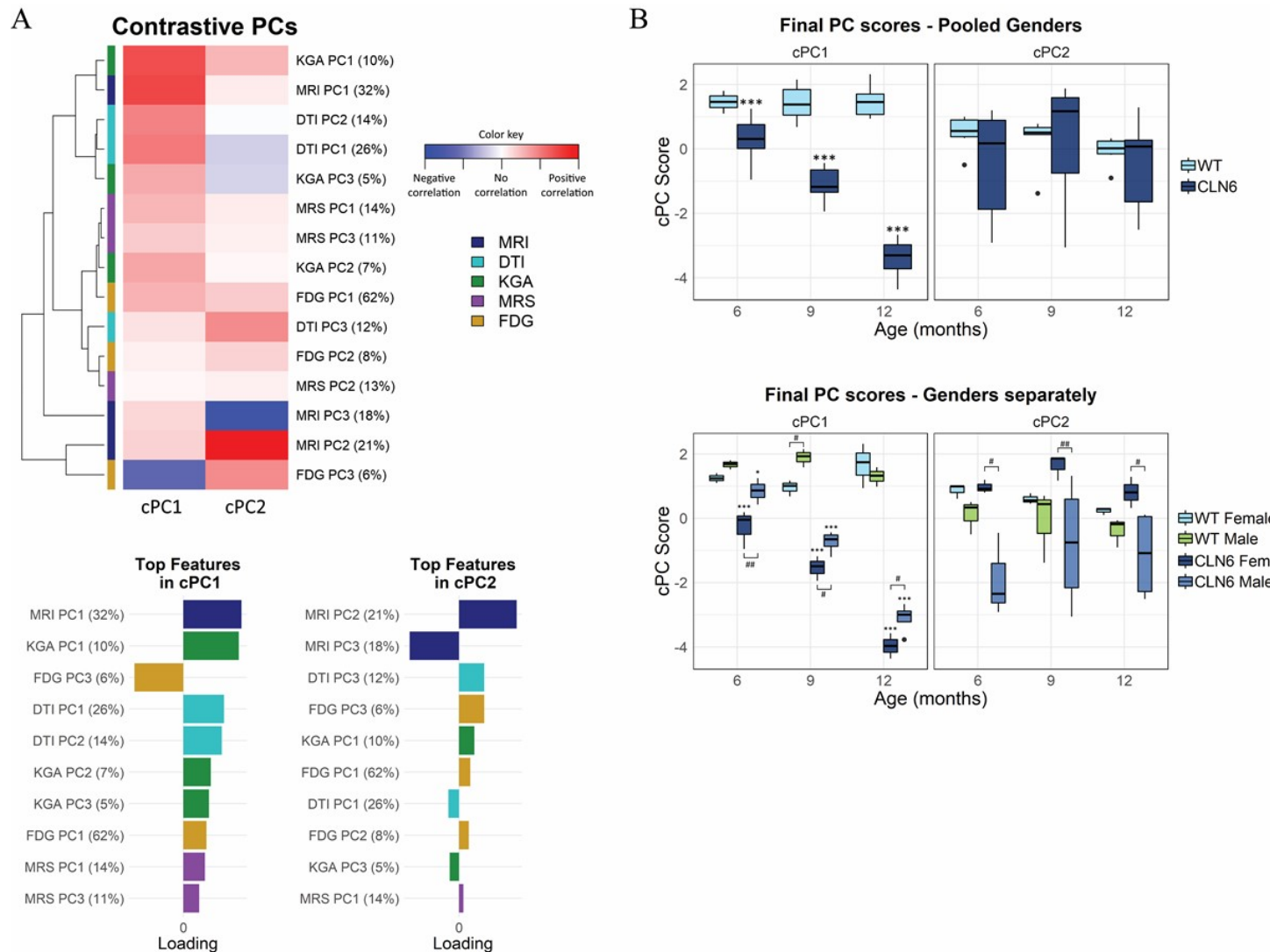


Fig. 5: Contrastive principal component analysis defines new variables that best capture the progressive changes present in the *Cln6^{nclf}* disease state. A) Contrastive principal components shown as heatmap. The most strongly correlated phase 1 components in the cPCs are presented as color coded bar graphs. B) Final principal component scores presented as boxplots, pooled sexes (top) and sexes separately (bottom). The first component, most emphasized by MRI PC1, KGA PC1, FDG PC1 and DTI PC1 and 2, demonstrate progressively increasing phenotype difference (*) in both sexes. The cPC2, consisting mostly of MRI PC1 and 2 but also DTI PC3 and FDG PC3, reveals sex difference (#) in *Cln6* mice at all ages. n = 6 for WT (3 male, 3 female), n = 7 for *Cln6^{nclf}* (4 male, 3 female). Statistical significances: unpaired t-test of estimated mean differences *p < 0.05, **p < 0.01, ***p < 0.001